

Streaming instability with multiple dust species – I. Favourable conditions for the linear growth

Zhaohuan Zhu(朱照寰)[✉]★ and Chao-Chin Yang(楊朝欽)[✉]

Department of Physics and Astronomy, University of Nevada, Las Vegas, 4505 S. Maryland Parkway, Box 454002, Las Vegas, NV 89154-4002, USA

Accepted 2020 November 17. Received 2020 October 27; in original form 2020 July 31

ABSTRACT

A recent study suggests that the streaming instability, one of the leading mechanisms for driving the formation of planetesimals, may not be as efficient as previously thought. Under some disc conditions, the growth time-scale of the instability can be longer than the disc lifetime when multiple dust species are considered. To further explore this finding, we use both linear analysis and direct numerical simulations with gas fluid and dust particles to mutually validate and study the unstable modes of the instability in more detail. We extend the previously studied parameter space by one order of magnitude in both the range of the dust-size distribution $[T_{s, \min}, T_{s, \max}]$ and the total solid-to-gas mass ratio ε and introduce a third dimension with the slope q of the size distribution. We find that the fast-growth regime and the slow-growth regime are distinctly separated in the ε – $T_{s, \max}$ space, while this boundary is not appreciably sensitive to q or $T_{s, \min}$. With a wide range of dust sizes present in the disc (e.g. $T_{s, \min} \lesssim 10^{-3}$), the growth rate in the slow-growth regime decreases as more dust species are considered. With a narrow range of dust sizes (e.g. $T_{s, \max}/T_{s, \min} = 5$), on the other hand, the growth rate in most of the ε – $T_{s, \max}$ space is converged with increasing dust species, but the fast and the slow growth regimes remain clearly separated. Moreover, it is not necessary that the largest dust species dominate the growth of the unstable modes, and the smaller dust species can affect the growth rate in a complicated way. In any case, we find that the fast-growth regime is bounded by $\varepsilon \gtrsim 1$ or $T_{s, \max} \gtrsim 1$, which may represent the favourable conditions for planetesimal formation.

Key words: hydrodynamics – instabilities – planets and satellites: formation – protoplanetary discs.

1 INTRODUCTION

One major obstacle for planet formation under the core accretion scenario is how solids can grow from cm/m-sized objects to km-sized planetesimals within a 1–10 Myr disc lifetime (Williams & Cieza 2011; Ansdell et al. 2016). Dust can grow from the interstellar medium (ISM) μm sizes to mm/cm sizes via electrostatic forces at collisions. Objects of km sizes and above can bind themselves and accrete materials via their own gravity (Benz & Asphaug 1999; Leinhardt & Stewart 2009; Bukhari Syed et al. 2017; San Sebastián et al. 2020). However, it is difficult for solids to grow from pebble sizes to km sizes (Johansen et al. 2014). Collisions between dust at these sizes often lead to bouncing or fragmentation instead of growth (Blum & Wurm 2008; Zsom et al. 2010). Furthermore, mm/cm-sized pebbles in the outer disc or metre-sized boulders in the inner disc radially drift inward problematically fast in protoplanetary discs. In a smooth disc, these solids should drift to the central star within $\sim 10^4$ yr, which is known as the radial-drift barrier for planetesimal formation (Adachi, Hayashi & Nakazawa 1976; Weidenschilling 1977; Brauer, Dullemond & Henning 2008; Birnstiel, Fang & Johansen 2016).

Several mechanisms have been proposed to overcome these barriers to the planetesimal formation, including dust traps at a local pressure maximum (Whipple 1972; Johansen, Youdin & Klahr 2009; Bai & Stone 2014) or within vortices (Barge & Sommeria 1995; Lyra et al. 2009), growth of porous icy dust aggregates (Kataoka et al.

2013), secular gravitational instability (Youdin 2011; Michikoshi, Kokubo & Inutsuka 2012; Takahashi & Inutsuka 2014), and the streaming instability (Youdin & Goodman 2005; Johansen & Youdin 2007; Youdin & Johansen 2007; Lin & Youdin 2017). Among these, the streaming instability is one promising mechanism to concentrate dust particles of a wide range of sizes (Carrera, Johansen & Davies 2015; Yang, Johansen & Carrera 2017; R. Li et al., in preparation). Unlike other mechanisms, which passively rely upon the underlying disc structures, dust particles actively participate in the dust–gas dynamics and spontaneously concentrate themselves via the reaction of the aerodynamic drag back on to the gas (Yang & Johansen 2014; Li, Youdin & Simon 2018).

However, Krapp et al. (2019) found that the linear growth of the streaming instability can be significantly different when considering a range of dust sizes instead of a single dust species as in previous studies. For some dust-size distributions and total solid-to-gas mass ratios, the growth rate of the instability decreases with an increasing number of discrete species representing the distribution. It appears that for these cases, the growth time-scale can be much longer than the typical disc lifetime for large number of dust species. This implies that taking the limit of a continuous dust-size distribution, the instability may not operate at all in protoplanetary discs. On the other hand, previous stratified numerical simulations (Bai & Stone 2010; Schaffer, Yang & Johansen 2018) have indicated that the streaming instability with multiple dust sizes appears to operate in these stratified discs and can even drive a strong concentration of dust particles. Furthermore, the effects of background turbulence have not been considered in this scenario yet (Yang, Mac Low & Johansen 2018; Chen & Lin 2020; Umurhan, Estrada & Cuzzi 2020), and it

* E-mail: zhaohuan.zhu@unlv.edu

appears that turbulence may play an important role in determining the efficiency and scale of planetesimal formation (Gerbig et al. 2020; Gole et al. 2020; Klahr & Schreiber 2020). Therefore, further studies of the multispecies streaming instability seem warranted.

In this work, we augment the study by Krapp et al. (2019) as follows. We validate the linearly unstable modes of the instability by using both linear analysis and direct numerical simulations (Section 2). We expand the parameter space by one order of magnitude in both the range of dust sizes and the total solid-to-gas ratio, and moreover, we explore the effects of the slope of the dust-size distributions (Section 3). Then, we discuss the properties of the most unstable mode (Section 4.1), the contributions from different dust species (Section 4.2), long-wavelength modes in a special region of the parameter space (Section 4.3), and the instability with a narrow dust size distribution (Section 4.4). Finally, we briefly summarize our results (Section 5).

2 METHODS

2.1 Linear analysis

We carry out the linear analysis for the multispecies streaming instability using the linearized perturbation equations presented in Appendix E of Benítez-Llambay, Krapp & Pessah (2019), which assumes no vertical stratification and no background turbulence. The underlying dust-size distribution is assumed to follow a power law $dn(s)/ds \propto s^q$ (Mathis, Rumpl & Nordsieck 1977) from s_{\min} to s_{\max} , where s is the size of the dust particle. Since dust particles under the conditions of a typical protoplanetary disc are mostly in the Epstein regime (e.g. Johansen et al. 2014), we assume that the dimensionless stopping time (T_s) of the particles is proportional to their size.

Under these assumptions, we consider dust with sizes from $T_{s,\min}$ to $T_{s,\max}$ (i.e. $T_s \in [T_{s,\min}, T_{s,\max}]$) and a total dust-to-gas mass ratio of ε in a disc. To discretise the continuous distribution into N_{sp} dust species, we divide the dust distribution into N_{sp} bins uniformly in the $\log T_s$ space. The dust particles in each bin have identical stopping time $T_{s,i}$, being at the linear centre of the bin. The dust-to-gas mass ratio for each bin is

$$\varepsilon_i = \frac{T_{s,i,u}^{4+q} - T_{s,i,l}^{4+q}}{T_{s,\max}^{4+q} - T_{s,\min}^{4+q}} \varepsilon, \quad (1)$$

where $T_{s,i,u}$ and $T_{s,i,l}$ are the upper and lower dust size limits for each dust bin. With equation (1), $\varepsilon = \sum_i \varepsilon_i$, and hence when we increase the number of species N_{sp} with the same distribution, the total mass of the dust remains constant.

Under the local-shearing-box approximation, Benítez-Llambay et al. (2019) derived the equations describing the gas and N_{sp} dust species in the radial-vertical (xz) plane assuming axisymmetry. The linearized equations have been written in terms of the perturbed variables $\delta \hat{f}(k_x, k_z) e^{i(k_x x + k_z z) - \omega t}$ in the Fourier space. The wavenumber (k_x, k_z) and the complex eigenvalue $\omega(k_x, k_z)$ can be expressed in the dimensionless form of $K_i = k_i \eta R_0$ with $i = x, z$ and $\bar{\omega} = \omega / \Omega_K(R_0)$, where η is related to the radial pressure gradient at the orbital radius $R = R_0$ by

$$\eta \equiv \frac{h_0^2}{2} \frac{d \log P}{d \log R} \bigg|_{R_0}, \quad (2)$$

$h_0 \equiv H_0/R_0$ with H_0 being the disc scale height at R_0 , and $\Omega_K(R)$ is the Keplerian angular frequency (Nakagawa, Sekiya & Hayashi 1986). We choose $\eta v_K/c_s = 0.05$ as our fiducial radial pressure gradient, where $v_K = R\Omega_K$ and c_s are the Keplerian velocity and the local speed of sound at R_0 , respectively. We have also tried $\eta v_K/c_s = 0.1$

for the outer disc, but the results are almost identical to those with the fiducial gradient. The eigenvalues ω of the linearized equations are computed using Python NUMPY function `linalg.eigvals`, and the growth rate of the multispecies streaming instability is hence $\sigma = -\text{Re}(\omega)$. All growth rates σ presented in this article is normalized by Ω_K . We have compared our growth rates to all linear calculations considered in Youdin & Johansen (2007) and Benítez-Llambay et al. (2019), and the agreement on the growth rate and each eigenmode is more than six significant digits.

We consider three different power-law indices $q = -3.5, -2.5$, and -1.5 for the dust-size distribution, motivated by protoplanetary disc observations and dust coagulation/fragmentation calculations (e.g. Klahr & Ercolano 2012; Pérez et al. 2015). The smallest dust particles are fixed at $T_{s,\min} = 10^{-4}$ or 10^{-3} for most cases, while we change $T_{s,\min}$ to be some fraction of $T_{s,\max}$ in Section 4.4. Given the maximum dust stopping time $T_{s,\max}$ and the total solid-to-gas mass ratio ε , we calculate the maximum growth rate from all the eigenmodes for each K_x and K_z . We then search for the maximum growth rate among the Fourier space (K_x, K_z). This space is infinite, so we need to confine our search in practice. Youdin & Goodman (2005) have suggested that $K_x \sim K_z \sim 1/T_s$ is roughly where the fastest growing mode is for the single-species streaming instability. Therefore, centred around $K_x = K_z = 1/T_{s,\max}$, we uniformly choose 54 values of $\log_{10} K_x$ in $[A - 1.5, A + 2.5]$ and 54 values of $\log_{10} K_z$ in $[A - 3, A + 3]$, where $A \equiv -\log_{10} T_{s,\max}$. By inspection, we find that this domain size generally captures the absolute maximum of the growth rate. We notice though that the fastest growing mode for some cases has appreciably small K_x and K_z with respect to $1/T_{s,\max}$ (Section 4.1). Thus, we consider a different domain size for these cases with $\log_{10} K_x$ in $[A - 3, A + 2]$ and $\log_{10} K_z$ in $[A - 5, A + 2]$ in Section 4.3. Finally, we define the maximum growth rate σ for any given $T_{s,\max}$ and ε as the maximum among the 54×54 computed growth rates. Due to the high computational cost of solving the eigenvalue problem for up to 1024 dust species, we decide to limit to 54×54 values for the large K_x - K_z space. Furthermore, Krapp et al. (2019) noticed some fine structures in the K_x - K_z growth rate map with multiple dust species in the disc. Although our wavenumber resolution and the potential fine structures have little effect on the maximum growth rate, they can affect the exact values of K_x and K_z for the fastest growing mode, which may lead to minor non-smooth profiles in some of our figures.

For each given dust distribution, we systematically increase the number of dust species N_{sp} from 2 to 1024 and use the aforementioned method to find the maximum growth rate σ for each N_{sp} . However, the linear algebra becomes quite computationally intensive when N_{sp} is more than 1024. To estimate the maximum growth rate with more dust species (e.g. $N_{\text{sp}} = 2048$ and 4096), therefore, we simply use the K_x and K_z of the fastest growing mode found with 1024 dust species and only calculate the growth rate for this combination of K_x and K_z for 2048 and 4096 dust species, leading to our σ_{2048} and σ_{4096} , respectively. Our experience with $N_{\text{sp}} \leq 1024$ is that, in most cases, increasing N_{sp} does not change the wavenumber of the fastest growing mode, so our approach should give a good approximation of the maximum growth rate with 2048 and 4096 dust species. However, the fastest growing mode in some cases do change location in the K_x - K_z space when we increase the number of dust species (Section 4.1 and 4.2). Thus, we focus on σ_{1024} in this work and cautiously present results for σ_{2048} and σ_{4096} where they are available.

2.2 Numerical validation

In addition to linear analysis, we use a simulation code to reproduce a linear mode for several cases, which serves for two purposes. First,

the results from our linear analysis and the code are mutually validated, and in this process, we demonstrate the resolution requirement for simulating the streaming instability with multiple dust species. Second and perhaps more importantly, by using a code equipped with Lagrangian dust particles, we can gauge the validity of the multifluid approximation for dust particles used in the linear analysis, especially for relatively large ones ($T_s \sim 1$, Garaud, Barrière-Fouchet & Lin 2004) which also happen to have the highest growth rates.

For these purposes, we use the PENCIL CODE¹ (Brandenburg & Dobler 2002). It employs sixth-order finite differences to approximate any spatial derivatives and integrates the system of (magneto)hydrodynamical equations in time using third-order Runge–Kutta method. To stabilize the scheme, we use sixth-order hyper-diffusion with fixed Reynolds number (Yang & Krumholz 2012). The dust component is modelled as Lagrangian superparticles, and their trajectories are integrated in tandem with the Runge–Kutta steps. The drag interaction between each dust particle and its surrounding gas is achieved via the standard particle-mesh method (Youdin & Johansen 2007).

For each dust distribution $[T_{s,\min}, T_{s,\max}]$ and total solid-to-gas density ratio ε we explore, we select a mode with a wavenumber $K_x = K_z$ that is close to the fastest growing mode. We normalize the eigenvector such that the amplitude of the perturbation in total particle density relative to the equilibrium density is about 10^{-6} . We use a square computational domain that accommodates one wavelength per dimension. While it is straightforward to seed the mode in the gas component with Eulerian formulation, it is not trivial to do so in the dust component with Lagrangian superparticles. We describe in detail in Appendix A the algorithm of how to position the particles to focus the perturbations on to a desired mode. The velocities of the particles are then assigned according to their positions. For all cases, we allocate four particles per species per cell.² With that, we conduct each simulation up to a time on the order of one e -folding time, and measure the growth rate of the mode in each field and compare it with the theoretical growth rate obtained from the linear analysis.

3 TWO REGIMES OF THE INSTABILITY

We explore the 3D parameter space spanned by the maximum dust stopping time $T_{s,\max}$, the total solid-to-gas mass ratio ε , and the power-law index q for the dust-size distribution. For our main set of calculations, we fix the minimum dust size with $T_{s,\min} = 10^{-4}$, select 21 different $\log_{10} T_{s,\max}$ values from -3 to 1 and 16 different $\log_{10} \varepsilon$ values from -2 to 1 . Therefore, both our $T_{s,\max}$ and our ε are one order of magnitude larger than those investigated by Krapp et al. (2019). Furthermore, we expand their parameter study with a third dimension by considering three different $q = -3.5, -2.5$, and -1.5 . We describe our findings in this section.

3.1 Characteristic conditions

The top left-hand panel in Fig. 1 shows the maximum growth rate σ_{1024} for 1024 dust species following the dust-size distribution with the power-law index $q = -3.5$. Restricting our attention to the

parameter space of $T_{s,\max} \leq 1$ and $\varepsilon \leq 1$, we have reproduced the growth rate found by Krapp et al. (2019) (see their fig. 5). The growth rate generally increases with increasing ε . Two distinct regimes appear separated by roughly $\varepsilon \sim 0.3$, above which the growth rate of the instability is high ($\sigma \gtrsim 0.01 \Omega_K$) and below which it is appreciably lower ($\sigma \ll 0.01 \Omega_K$). As we expand the parameter space up to $\varepsilon = 10$, we find that the trend continues, as σ increases with increasing ε . Moreover, we find that σ also increases with decreasing $T_{s,\max}$ above the transition. The maximum growth time-scale is shorter than the orbital time near our smallest $T_{s,\max} \simeq 10^{-3}$ and our largest $\varepsilon \simeq 10$.

More interestingly, as we increase the maximum dust size up to $T_{s,\max} = 10$, we find another transition zone where the maximum growth rate changes from low to high. As shown by the top left-hand panel in Fig. 1, this transition lies at roughly $T_{s,\max} \sim 1$. Therefore, it appears that high growth rate occurs when *either* the maximum size $T_{s,\max}$ *or* the total solid-to-gas mass ratio ε is high, while low growth rate occurs when *both* $T_{s,\max}$ *and* ε are low.

We further investigate the effects of changing the slope of the dust-size distribution. The top panels in Fig. 1 compare the maximum growth rate σ_{1024} for different power-law index q , with flatter size distribution (more top heavy) toward the right (see equation 1). As shown by the panels, the general trend found above remains the same, while there are only slight changes of the transition zone separating fast and slow growth of the instability. With a more top-heavy dust distribution, the transition at $\varepsilon \sim 1$ becomes less sensitive to $T_{s,\max}$, and there is a slightly larger parameter space at $T_{s,\max} \sim 1$ for high growth rates. On the other hand, the most unstable modes for cases at $0.1 \lesssim T_{s,\max} \lesssim 1$ have small K_z which may not fit into the disc thickness, which we discuss in more detail in Section 4.1.

After studying the effects of $T_{s,\max}$ and q on the instability growth rate, we explore the effects of $T_{s,\min}$ by increasing $T_{s,\min}$ from 10^{-4} to 10^{-3} . The resulting growth rates are shown in Fig. 2. By comparing Fig. 2 with Fig. 1, we find that the growth rate is not appreciably changed by $T_{s,\min}$ as long as $T_{s,\max}$ is not close to $T_{s,\min}$. We investigate the special cases with $T_{s,\max}$ close to $T_{s,\min}$ in Section 4.4. For the convenience of direct numerical simulations with which time-steps are constrained by the small dust species, we use $T_{s,\min} = 10^{-3}$ to validate the unstable modes in several representative cases in Fig. 2 (triangles in the figure), as presented in Section 3.3.

3.2 Transition between the converged and non-converged regimes

As discovered by Krapp et al. (2019), the fast and slow growth regimes discussed in Section 3.1 also seem to have distinct growth rate convergence with the number of discrete dust species N_{sp} representing the distribution. Although we find that such connection between the fast (or slow) growth and converged (or non-converged) growth rate can break down for discs with a narrow dust size distribution (e.g. $T_{s,\min} \gtrsim 0.1 T_{s,\max}$; see Section 4.4), the distinctly different properties of convergence between the two regimes remain apparent for dust distributions with a wide size range. For $T_{s,\min} = 10^{-3}$ and 10^{-4} cases, the growth rate in the fast-growth regime converges to a finite value, while in the slow-growth regime, the growth rate appears to approach zero, i.e. the system seems to be virtually stable to the streaming instability. In this section, we attempt to identify the transition between these two regimes.

In the middle panels of Figs 1 and 2, we plot the ratio between σ_{1024} and σ_{512} for the same parameters as in the top panels. This ratio decreases quickly from one (converged rates, which corresponds to the red colour) to ~ 0.5 (blue colour) as either ε or $T_{s,\max}$ decreases across some critical values. The transition zone separating the two

¹The PENCIL CODE and its documentation is publicly available at <http://pencil-code.nordita.org/>.

²We find that with one particle per species per cell, grid noise of small amplitudes appear at high resolutions. Using four particles per cell effectively eliminates this noise.

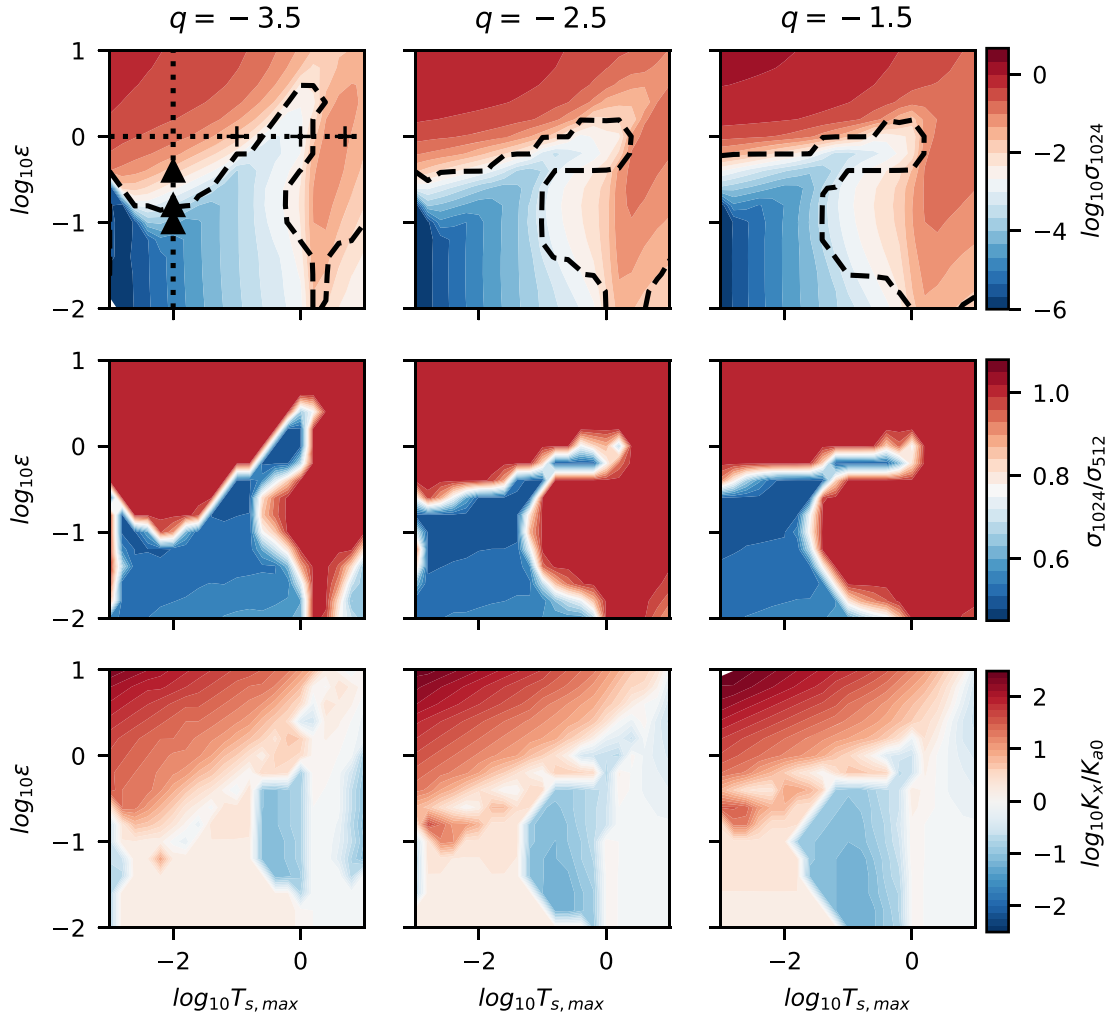


Figure 1. Maximum growth rate σ (in Ω_K) of the multispecies streaming instability for discs with different maximum dust size at $T_{s, \max}$, total solid-to-gas mass ratio ϵ , and power-law index q of the dust-size distribution. $T_{s, \min}$ is fixed at 10^{-4} . The higher q (less negative), the more top heavy the distribution is. The upper panels show the rate with 1024 dust species σ_{1024} . The middle panels show the ratio between the rates with 1024 and 512 dust species $\sigma_{1024}/\sigma_{512}$. The dashed lines in the upper panels denote $\sigma_{1024}/\sigma_{512} = 0.99$. The dotted lines are the 1D cuts analyzed in Section 3.2. The triangles and the crosses mark the parameter sets studied in Section 4.1. The bottom panels show the radial component of the dimensionless wavenumber K_x of the fastest growing mode with 1024 dust species. K_x is normalized by K_{a0} (equation 3).

regimes appears to be excessively sharp, and thus we overplot the contour of $\sigma_{1024}/\sigma_{512} = 0.99$ with dashed curves in the top panels to mark this transition. If $\sigma_{2N_{sp}}/\sigma_{N_{sp}} \simeq 1$, the growth rate should approach to a finite value, while if $\sigma_{2N_{sp}}/\sigma_{N_{sp}} < 1$, the growth rate will continue to approach to zero as N_{sp} increases. Therefore, with more and more dust species, we can expect that the growth rate remains the same in the upper and right sides of the dashed curve, while the growth rate below the dashed curve continues to decrease so that the blue region in the top panels (σ panels) will become darker and darker, i.e. $\sigma_{N_{sp}} \ll 1$.

The bottom panels in Figs 1 and 2 show the K_x of the fastest growing mode. The K_x value is normalized to K_{a0} . K_{a0} represents the K_x of the fastest growth mode for a single dust species having $T_s = T_{s, \max}$. Squire & Hopkins (2018) used the wave-drift resonance to show that the fastest growing short-wavelength mode for a single dust species with dust-to-gas mass ratio $\epsilon \lesssim 1$ and stopping time T_s occurs at

$$K_x = K_a \equiv \frac{(1 + \epsilon)^2 + T_s^2}{2(1 + \epsilon)T_s}. \quad (3)$$

When $\epsilon \ll 1$, K_a is insensitive to ϵ so that we use K_{a0} , which is K_a with $\epsilon = 0$, to scale K_x . We see that the converged and non-converged regimes have very different fastest growing modes, and we analyse them in more detail in Section 4.1.

To study how sharp this transition between the two regimes is, we conduct two additional sets of calculations. For one set, we fix $T_{s, \max} = 0.01$ while varying ϵ with 192 different values from 10^{-2} to 10. For the other set, we fix $\epsilon = 1$ while varying $T_{s, \max}$ with 192 different values from 10^{-3} to 10. For both sets, we consider only the dust-size distribution with power-law index $q = -3.5$. The trace of these two fine scans are schematically drawn with the two dotted lines in the top left-hand panel of Fig. 1, and the resulting maximum growth rates are shown in Figs 3 and 4, respectively. The number of dust species N_{sp} increases from 256 in the left-hand panels to 4096 in the right-hand panels.³

³We caution that the growth rates for 2048 and 4096 species are calculated at the same wavenumber (K_x , K_z) of the fastest growing mode for 1024 species (Section 2.1).

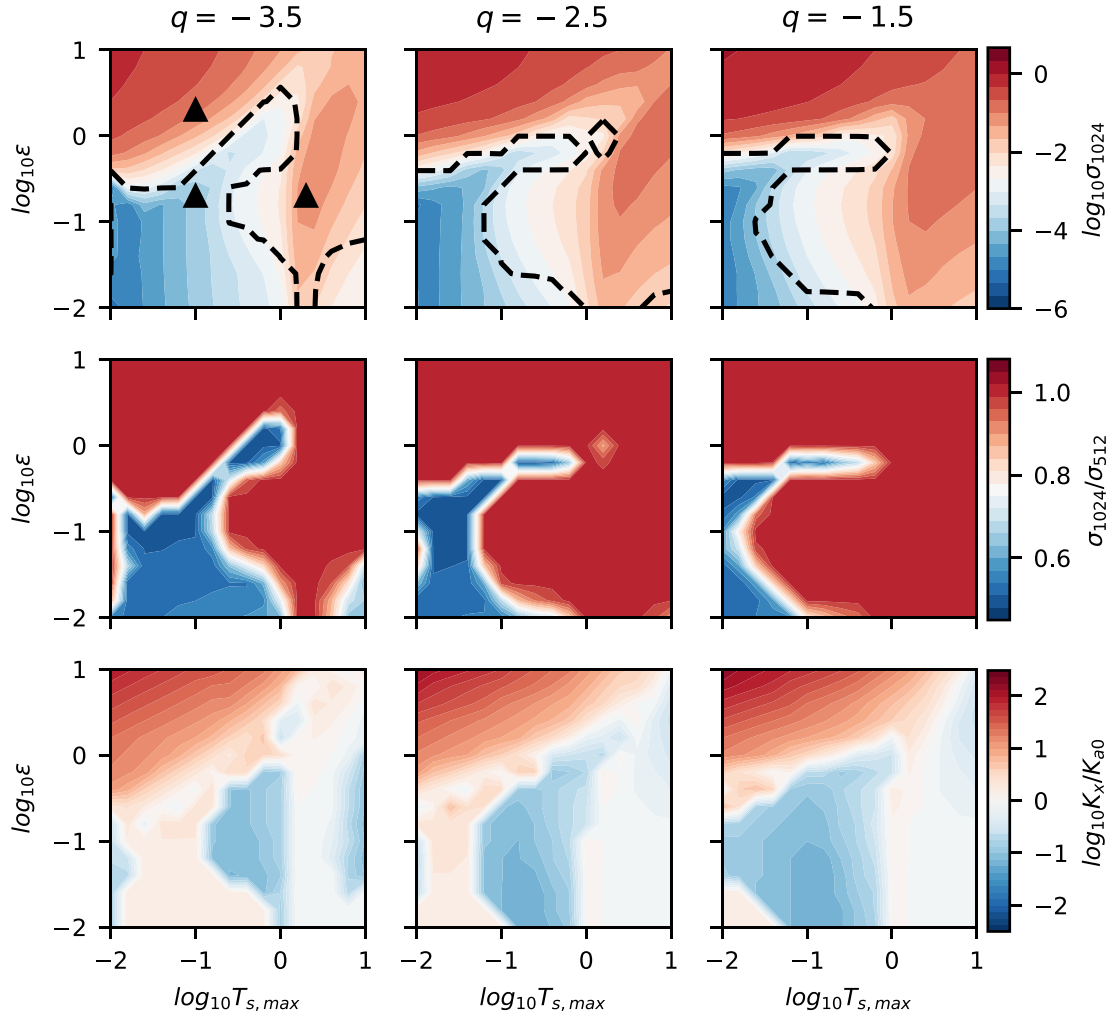


Figure 2. Similar to Fig. 1 but with the minimum dust size $T_{s, \min} = 10^{-3}$. The three triangles in the top left-hand panel denote the three cases which we have tested using direct numerical simulations (Section 3.3).

As shown by the bottom panels of Fig. 3, the growth rate converges with the number of dust species to finite values ($\sigma_{2N_{sp}}/\sigma_{N_{sp}} = 1$) for $T_s \in [10^{-4}, 10^{-2}]$ and $\varepsilon \gtrsim 0.1$. The transition from $\sigma_{2N_{sp}}/\sigma_{N_{sp}} \sim 0.5$ to $\sigma_{2N_{sp}}/\sigma_{N_{sp}} = 1$ becomes sharper and sharper with increasing N_{sp} , which can also be seen in the upper panels. While the growth rate for $\varepsilon \gtrsim 0.1$ remain the same from the left to the right top panels (increasing N_{sp}), the growth rate for $\varepsilon \lesssim 0.1$ becomes smaller and smaller. This leads to a discontinuity of the growth rate which can be identified as the boundary between the two regimes. With larger number of dust species, the fast-growth regime remains to have high growth rate while the slow-growth regime has decreasingly low growth rate.

We now consider the systems with a fixed $\varepsilon = 1$ and different $T_{s, \max}$, along the horizontal dotted line in the top left-hand panel of Fig. 1. The growth rate as a function of $T_{s, \max}$ is shown in the top panels of Fig. 4 with various N_{sp} . For $T_{s, \max} \lesssim 0.02$ and $T_{s, \max} \gtrsim 0.2$, the profile of the growth rate remains the same with increasing N_{sp} , as also evident in the bottom panels where $\sigma_{2N_{sp}}/\sigma_{N_{sp}} = 1$. For $0.02 \lesssim T_{s, \max} \lesssim 0.2$, on the contrary, the rate becomes lower and lower with increasing N_{sp} , leading to a growth rate orders of magnitude lower than in the fast-growth regime when $N_{sp} = 4096$. Similar to the case of fixed dust-size distribution but varying ε , the transitions at $T_{s, \max} \simeq 0.02$ and $\simeq 0.2$ become sharper and sharper with increasing N_{sp} .

Therefore, the two regimes appear to be distinctly separated by a well-defined boundary, as delineated by the dashed lines in Figs 1 and 2.

3.3 Numerical validation

As described in Section 2.2, we use the PENCIL CODE to mutually validate the eigenmodes derived from our linear analysis. We select three different dust distributions: (1) $T_s \in [10^{-3}, 0.1]$ and $\varepsilon = 2$, (2) $T_s \in [10^{-3}, 0.1]$ and $\varepsilon = 0.2$, and (3) $T_s \in [10^{-3}, 2]$ and $\varepsilon = 0.2$, all of which have a power-law index of $q = -3.5$. For each distribution, we choose an eigenmode with a wavenumber $K_x = K_z$ that is close to the fastest growing mode. The three cases are marked by the triangles in Fig. 2, and the growth rate of the mode as a function of number of dust species N_{sp} is listed in Table 1.

First, we consider the distribution $T_s \in [10^{-3}, 0.1]$ and $\varepsilon = 2$. As shown in Fig. 2, this case belongs to the converged fast-growth regime. The growth rate approaches to a constant with increasing number of dust species and convergence occurs at $N_{sp} \sim 16$, as indicated by Table 1. Fig. 5 shows the growth rate measured by the PENCIL CODE with various N_{sp} and resolutions λ/Δ , where $\lambda = 2\pi/k_i$ is the wavelength per dimension with $i = x, z$, and Δ is the grid spacing. The simulation data demonstrate convergence with

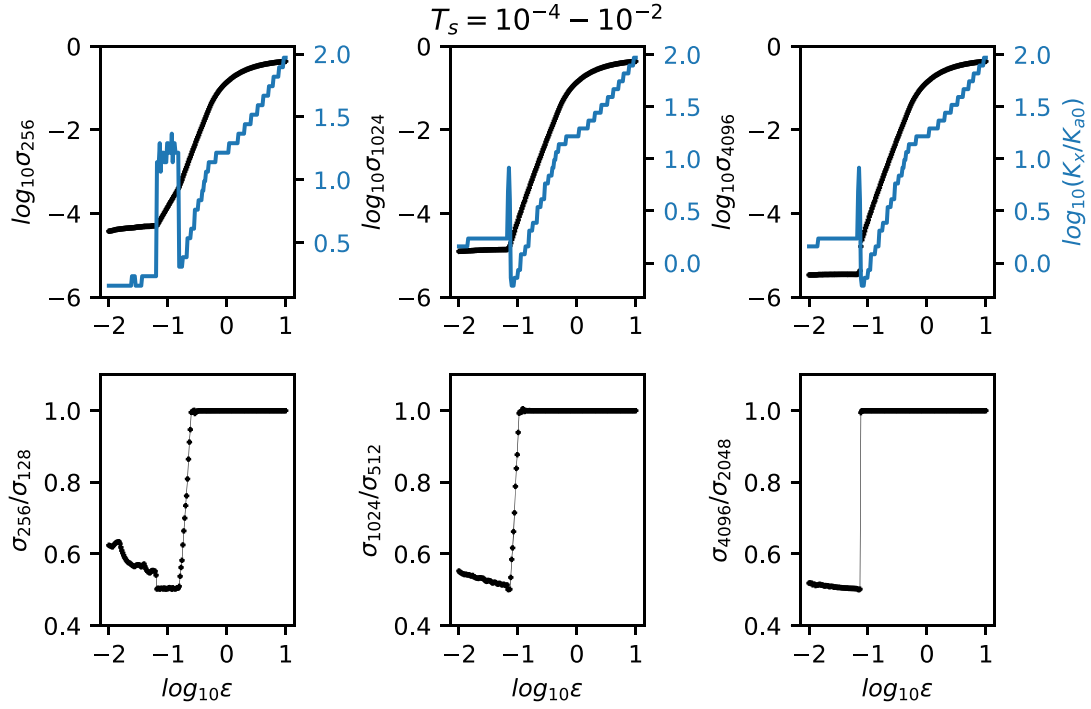


Figure 3. The growth rate $\sigma_{N_{\text{sp}}}$ (in Ω_K) and the dimensionless radial wavenumber K_x of the fastest growing mode (top panels) and the growth rate ratio $\sigma_{2N_{\text{sp}}}/\sigma_{N_{\text{sp}}}$ (bottom panels) as a function of the total dust-to-gas mass ratio ε for discs with a dust distribution of $T_s \in [10^{-4}, 10^{-2}]$ and $q = -3.5$ (along the vertical dotted line in the top left-hand panel of Fig. 1). Number of dust species N_{sp} representing the distribution increases from the left- to the right-hand panels.

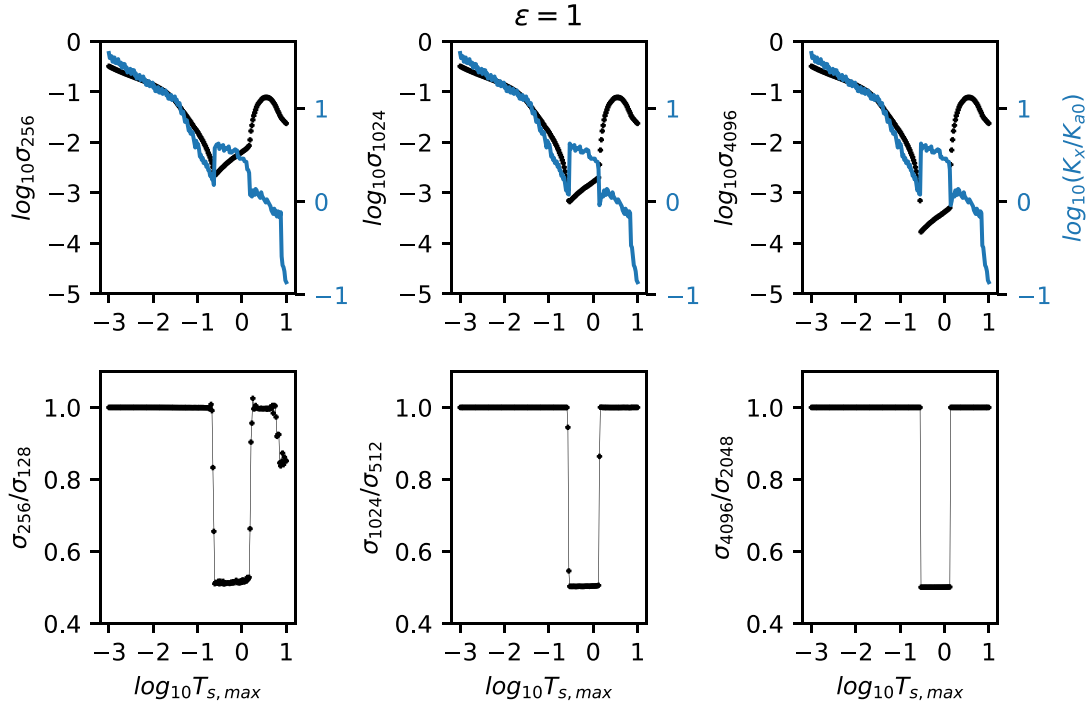


Figure 4. The growth rate $\sigma_{N_{\text{sp}}}$ (in Ω_K) and the dimensionless radial wavenumber K_x of the fastest growing mode (upper panels) and the growth rate ratio $\sigma_{2N_{\text{sp}}}/\sigma_{N_{\text{sp}}}$ (bottom panels) as a function of the maximum size $T_{s,\text{max}}$ in a dust-size distribution with power-law index $q = -3.5$ (along the horizontal dotted line in the top left-hand panel of Fig. 1). The minimum size is $T_{s,\text{min}} = 10^{-4}$ and the total dust-to-gas mass ratio is fixed at $\varepsilon = 1$. Number of dust species N_{sp} representing the distribution increases from the left- to the right-hand panels.

Table 1. Growth rate σ (in Ω_K) of fast-growing eigenmode in multispecies streaming instability to be compared with direct numerical simulations.

N_{sp}	$T_s \in [10^{-3}, 0.1]$ $\varepsilon = 2$	$T_s \in [10^{-3}, 0.1]$ $\varepsilon = 0.2$	$T_s \in [10^{-3}, 2]$ $\varepsilon = 0.2$
	$K_x = K_z = 60$	$K_x = K_z = 10$	$K_x = K_z = 1$
1	0.400 922	0.007 481 44	0.088 557 0
2	0.061 607 3	0.007 877 42	0.085 747 7
4	0.169 425	0.006 150 58	0.079 473 7
8	0.127 082	0.003 341 11	0.051 961 3
16	0.097 617 7	0.002 831 22	0.057 368 3
32	0.098 025 0	0.001 695 62	0.045 001 6
64			0.038 604 3
128			0.039 724 9

resolution to the theoretical rate at each given N_{sp} . For $N_{sp} > 2$, convergence of gas velocity and dust density is seen at $\lambda/\Delta \sim 32$ while convergence of dust velocity and gas density is seen at $\lambda/\Delta \sim 64$. For the case of $N_{sp} = 1$, the convergence with resolution is similar while it is slightly worse for the case of $N_{sp} = 2$.

We next consider the dust distribution $T_s \in [10^{-3}, 0.1]$ and $\varepsilon = 0.2$. It only differs from the previous case by the much decreased solid-to-gas mass ratio ε , leading to longer critical wavelengths and into the non-converged slow-growth regime (Fig. 2). As shown by Table 1, the growth rate continues to decrease with an increasing number of dust species N_{sp} . Again we use the PENCIL CODE to measure the growth rate up to $N_{sp} = 32$ with varying resolutions, and the results are shown in Fig. 6. The code can still capture the instability accurately at such a low growth rate of $\sigma \simeq 0.0017\Omega_K$ and convergence with resolution can be seen at $\lambda/\Delta \sim 64$. For comparison, the LinB mode for the single-species streaming instability ($T_s = 0.1$ and $\varepsilon = 0.2$) has a growth rate of $\sigma \simeq 0.015\Omega_K$, the lowest ever used for code validation

in the previous literature (Youdin & Johansen 2007; Balsara et al. 2009; Bai & Stone 2010; Miniati 2010; Yang & Johansen 2016; Benítez-Llambay et al. 2019; Krapp et al. 2019; Mignone, Flock & Vaidya 2019). The case we validate here has a growth rate one order of magnitude lower and hence is more challenging.

Finally, we change the maximum size of the dust distribution from the previous case to $T_{s, \max} = 2$, the latter of which is in the converged fast-growth regime (Fig. 2). This case is valuable in the sense that the largest dust particles probe into the regime of $T_s \sim 1$, above which the fluid approximation used by the linear analysis may be broken because the trajectories of the particles may begin to cross (Garaud, Barrière-Fouchet & Lin 2004). The growth rate measured with the PENCIL CODE as a function of the number of dust species N_{sp} and the resolution λ/Δ is shown in Fig. 7. Once again, convergence of the growth rate to the theoretical rate with resolution at any given N_{sp} is achieved. The growth in the velocity and density field of the gas converges at $\lambda/\Delta \sim 16$ –32, while that of the dust particles converges at $\lambda/\Delta \sim 32$ –64. This experiment indicates that the fluid approximation for the dust particles is still valid in the linear growth of the instability for the largest particles up to $T_{s, \max} \sim 2$. However, it remains to be seen if the approximation holds valid in the non-linear saturation of the instability.

4 DISCUSSION

4.1 On the critical wavenumber

To explore further the nature of the instability in the fast/slow or converged/non-converged regimes, we turn our attention to the most unstable mode itself for any given system. Based on the linear analysis of the single-species streaming instability, Youdin & Goodman (2005) found that the most unstable mode occurs along

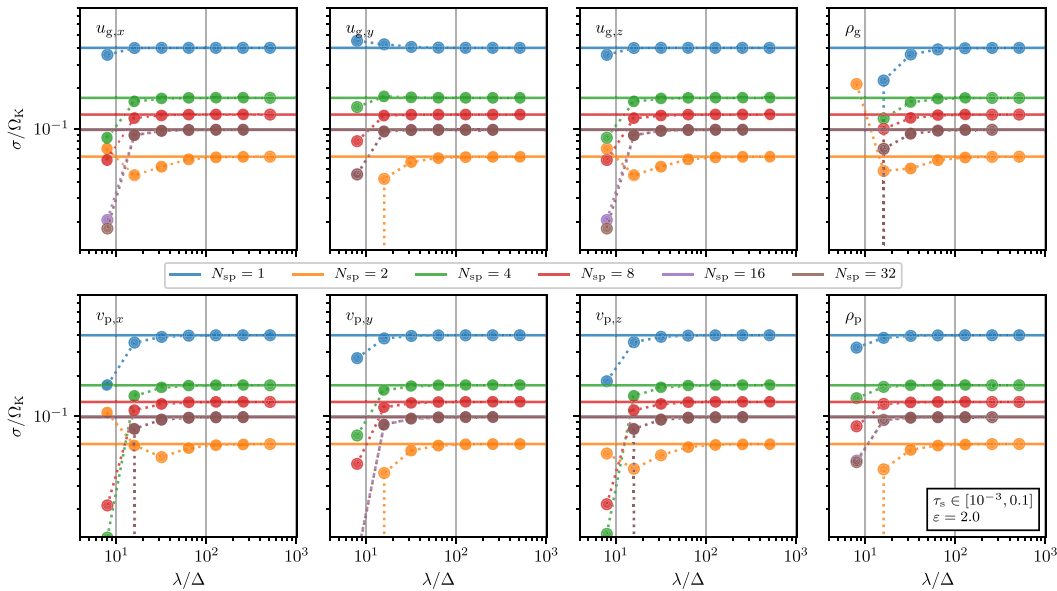


Figure 5. Numerical validation of linear modes of the streaming instability for different numbers of dust species using the PENCIL CODE. The dots are the growth rate σ of a mode in units of Ω_K , measured from the simulation data at various resolution in terms of number of grid points per wavelength λ/Δ . Different colours represent different numbers of dust species N_{sp} in the system. The solid lines are the theoretical growth rates. The top panels show the components of the velocity field and the density of the gas, while the bottom panels show the components of the mass-weighted velocity field and the total density of the dust particles. In this case, the dimensionless stopping time is in the range of $T_s \in [10^{-3}, 0.1]$, and the total solid-to-gas mass ratio is $\varepsilon = 2$. The selected mode has the wavenumber $K_x = K_z = 60$, which is close to the fastest growing mode. We note that the results are close to identical between the $N_{sp} = 16$ and the $N_{sp} = 32$ cases.

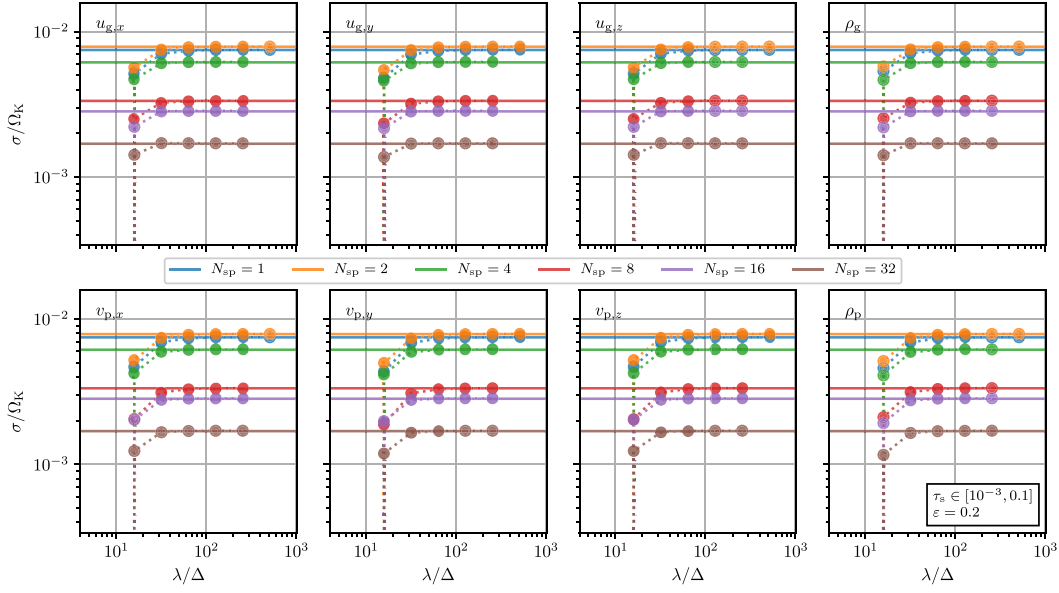


Figure 6. Same as Fig. 5, except that $\varepsilon = 0.2$ and $K_x = K_z = 10$.

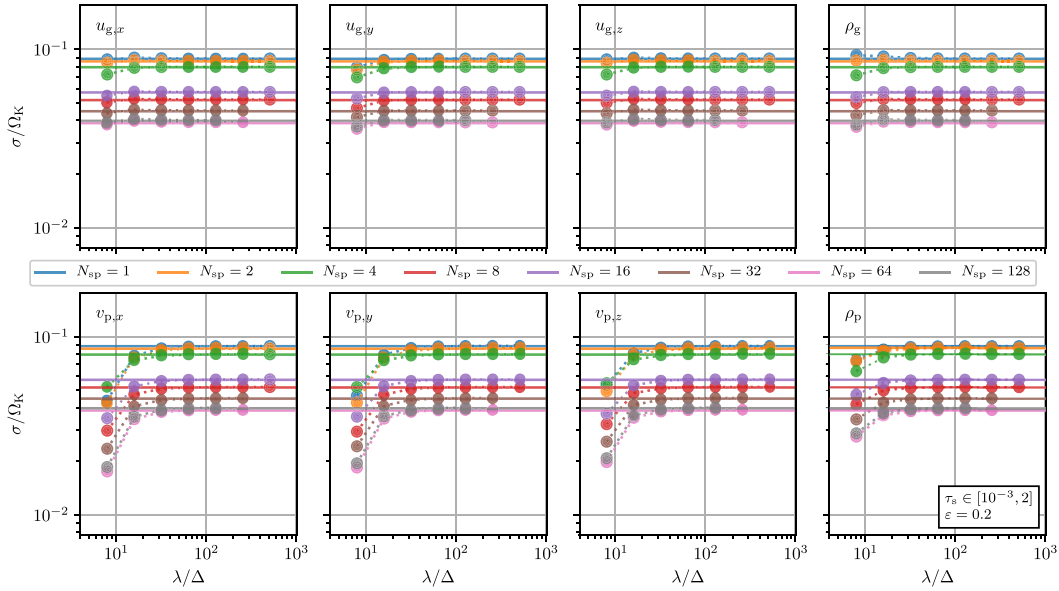


Figure 7. Same as Fig. 5, except that $T_s \in [10^{-3}, 2]$, $\varepsilon = 0.2$, and $K_x = K_z = 1$.

$K_z \sim T_s K_x^2$ on the long-wavelength side and $K_x \sim \text{constant}$ on the short-wavelength side, which are bridged roughly at $K_x \sim K_z \sim 1/T_s$. Usually, the maximum growth rate can be found near $K_x \sim K_z \sim 1/T_s$ or on the vertical $K_x \sim 1/T_s$. This property is closely related with the resonant drag instability, in which the relative drift velocity between the gas and the dust resonates with the projected wave speed of the gas (Squire & Hopkins 2018). With this new insight into the streaming instability, Squire & Hopkins (2018) gave a physically motivated K_x – K_z condition for the long-wavelength branch (their equation 33) and $K_x = K_a$ (equation 3) for the short-wavelength branch, assuming $\varepsilon \lesssim 1$ (see also Umurhan, Estrada & Cuzzi 2020). In the following, we use it as a reference to analyse what we find in the multispecies streaming instability.

The bottom panels in Figs 1 and 2 show K_x of the mode that has the highest growth rate. The dimensionless radial wavenumber K_x is normalized by K_{a0} . Therefore, if the fastest growing mode is near the vertical branch $K_x = K_{a0}$, the colour should be white in these panels, and it can be implied that the largest dust particles drive the instability in the white region. As shown by the panels, the non-convergent cases (which correspond to the blue region in the panels in the middle row) roughly have $K_x/K_{a0} \sim 1$ – 3 . The convergent cases can be divided by $\varepsilon \sim 1$. For $\varepsilon \gtrsim 1$, $K_x \gtrsim 10K_{a0}$. For $\varepsilon \lesssim 1$, K_x depends on the maximum stopping time $T_{s, \text{max}}$: When $T_{s, \text{max}}$ is small, the fast growing mode has $K_x \ll K_{a0}$ (the vertical wavenumber K_z is similarly small such that the modes may not fit within the disc thickness, as discussed below), and when $T_{s, \text{max}} \gtrsim 1$, $K_x \sim K_{a0}$.

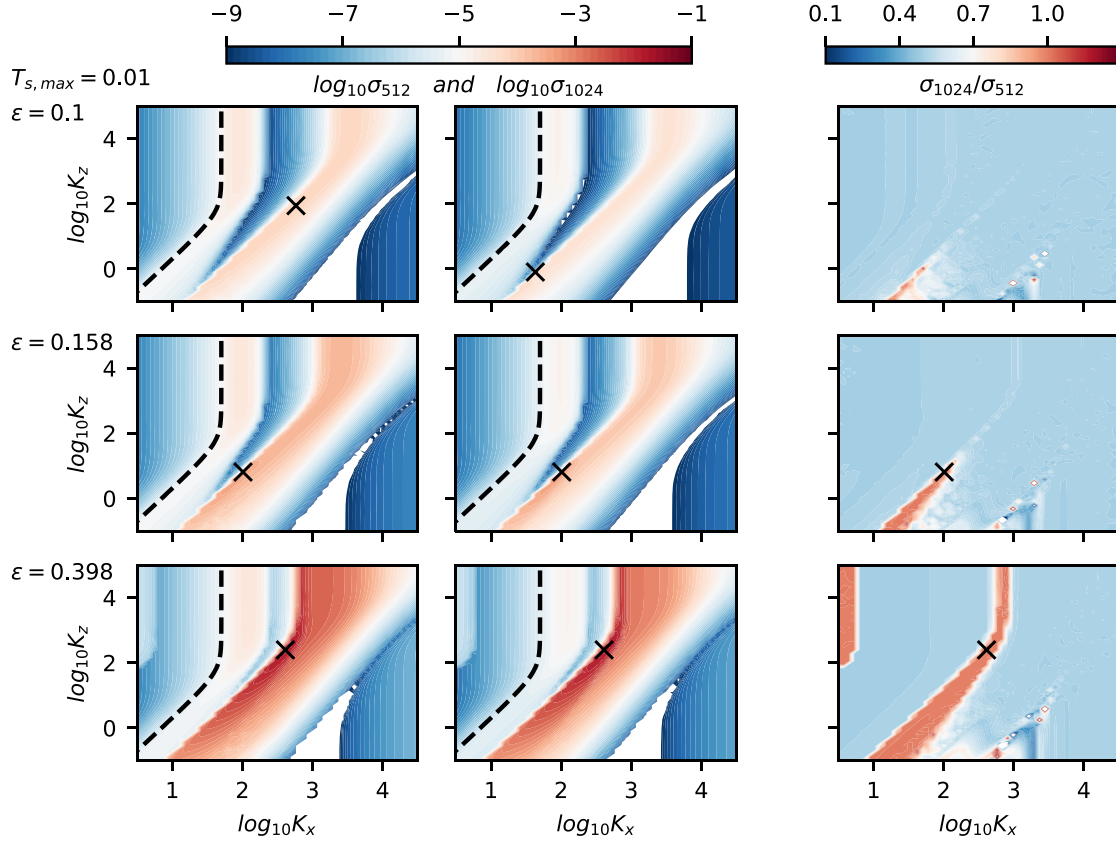


Figure 8. Growth rate of the most unstable mode σ (in Ω_K) as a function of the dimensionless wavenumber (K_x, K_z). The discs have the same dust distribution $T_s \in [10^{-4}, 10^{-2}]$ and $q = -3.5$, but the total solid-to-gas mass ratio ε increases from the top to the bottom panels. The three cases are represented by the triangles in the top left-hand panel of Fig. 1. The left-hand panels show the growth rate for discs with 512 dust species, while the middle panels show the growth rate for discs with 1024 dust species. The right-hand panels show the ratio between the left two panels. If the ratio at one point is one, the growth rate of that mode converges to finite values. The dashed curves in the left two columns are calculated using equation (33) in Squire & Hopkins (2018) near which the system with a single dust species having ε and $T_s = T_{s, \max}$ is the most unstable. The cross in each panel labels where the fastest growing mode is.

As in Section 3.2, we perform a vertical cut in the bottom left-hand panel of Fig. 1 as in the top left-hand panel, and plot K_x of the fastest growing mode (blue curves in Fig. 3) as a function of ε with a fixed dust distribution $T_s \in [10^{-4}, 10^{-2}]$ and $q = -3.5$. Similar to the convergence of the growth rate, we notice that K_x also has a dramatic change at the $\varepsilon \sim 0.1$ convergence boundary, indicating that non-convergent and convergent cases may have different types of the fastest growing modes. When $\varepsilon \lesssim 0.1$, K_x is close to $1-2K_{a0}$. At $\varepsilon \sim 0.1$, K_x jumps to $20K_{a0}$ for 256 dust species; for 1024 and 4096 dust species, there is only a narrow ε space for these high K_x values. For convergent cases with $\varepsilon \gtrsim 0.1$, K_x drops to $\sim K_{a0}$ and then increases with larger ε .

To study these modes in detail, we plot in Fig. 8 the growth rate with respect to K_x and K_z for three cases with the same $T_{s, \max}$ but different ε (located at the triangles in the top left-hand panel of Fig. 1). It can be seen that the fast growing modes (red coloured) may lie in two separate regions: the region that is close to the dust-gas drag resonance with single dust species $T_s = T_{s, \max}$ (dashed curves; Youdin & Goodman 2005; Squire & Hopkins 2018), and another region whose K_x is about one order of magnitude larger (which was also pointed out by Krapp et al. 2019). When ε is as small as ~ 0.01 (not shown), the fastest growing mode lies in the region that is close to the dashed curves. With larger $\varepsilon \sim 0.1$ (the uppermost panels of Fig. 8), the most unstable mode lies in the larger K_x region. As shown in the upper right-hand panel, both red regions do not show

convergent rates with increasing N_{sp} . Thus, the instability growth rate does not converge to finite values when $\varepsilon \lesssim 0.1$, consistent with Fig. 3. When ε continues to rise (the middle row in Fig. 8), the narrow region with $K_z \sim T_{s, \max} K_x^2/10$ and small K_x starts to show convergence and hence this region maintains its high growth rate with increasing N_{sp} (left and middle panels). This converged region extends to higher K_x and K_z when ε is even larger (the bottom panels). These changes of the convergent regions with ε explain the trend of K_x shown in Fig. 3.

We next consider the horizontal cut in the upper left-hand panel of Fig. 1, i.e. dust distributions with fixed $\varepsilon = 1$, $q = -3.5$, and $T_{s, \min} = 10^{-4}$ but with varying $T_{s, \max}$. The blue curves in the top panels of Fig. 4 show the radial wavenumber K_x of the fastest growing mode, and Fig. 9 shows the map of the growth rate with respect to K_x and K_z for three selected cases (located at the crosses in Fig. 1). For cases shown in both the top and the bottom panels of Fig. 9, the growth rate converges, while the growth rate does not converge for the case in the middle panels. The top panels show that when $T_{s, \max} \ll 1$, the fastest growing mode is at the large K_x branch. When $T_{s, \max}$ increases to ~ 1 , the convergent region shrinks significantly (right-hand panel), and the fastest growing mode occurs in the single-species resonant region $K_x \sim K_{a0}$ which does not show convergence with N_{sp} . When $T_{s, \max}$ increases to even larger values (e.g. $T_{s, \max} = 5$; the bottom panels), the fastest growing mode remains in this $K_x \sim K_{a0}$ region, but the region becomes converged with N_{sp} .

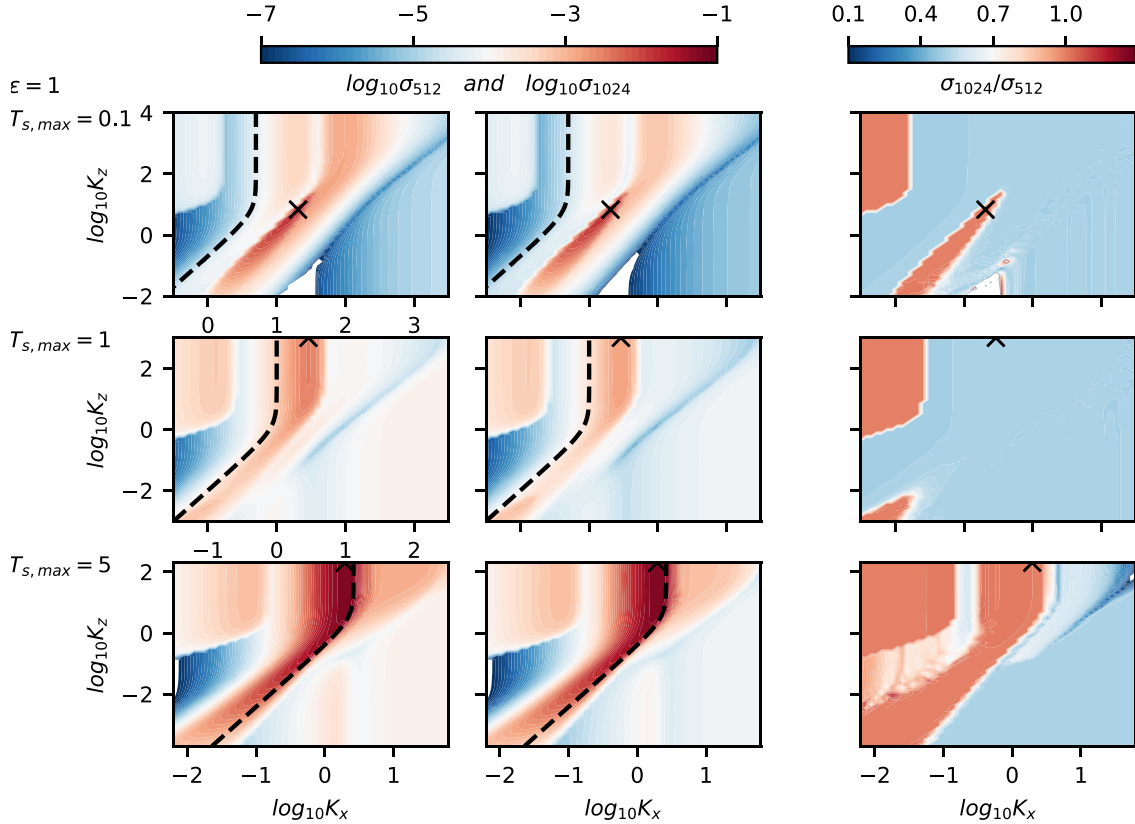


Figure 9. Similar to Fig. 8 but for discs with the same $\varepsilon = 1$ and $T_{s,\min} = 10^{-4}$ but varying $T_{s,\max}$. The value of $T_{s,\max}$ increases from the top to the bottom panels, and these cases are located at the three crosses in the top left-hand panel of Fig. 1.

Figs 8 and 9 show that unstable modes have converged growth rates with increasing N_{sp} in only a small region of the K_x – K_z space. If the fastest growing mode locates in this region, the growth rate of the instability converges to finite values with N_{sp} . The $K_x \sim K_{a0}$ region where the single-species streaming instability has the fastest growth rates sometimes does not show convergence with N_{sp} . Instead, a different region with larger K_x can converge under some $T_{s,\max}$ and ε conditions. For future analytical studies, it will be crucial to understand why the growth rate of unstable modes at any given K_x and K_z do or do not converge with N_{sp} .

Finally, we note that when the vertical wavenumber of the most unstable mode $k_z \lesssim 1/H_0$, the wavelength of the mode is larger than the disc thickness and thus the instability may not operate in the disc. Since $K_z = k_z \eta R_0$ and $\eta v_K/c_s = 0.05$, K_z of the unstable mode needs to be larger than 0.05 to fit into the disc. Thus, in Fig. 10, we only include modes with $K_z \geq 0.05$ for the computation of the maximum growth rate. Compared with Fig. 1, it can be seen that the converged region shrinks around $T_{s,\max} \sim 1$ and $\varepsilon \lesssim 1$, and the boundary between the convergent and the non-convergent regions is more aligned with $T_{s,\max} \sim 1$. This difference can be understood by inspecting the K_x values of the most unstable mode in the lower panels of Fig. 1, where K_x can become much less than K_{a0} around $T_{s,\max} \sim 1$. Since $K_z \sim K_x$ for these fastest growing modes, this implies that K_z can be so small around $T_{s,\max} \sim 1$ that the modes can be too large to fit in the disc.

4.2 Interaction between dust species

Krapp et al. (2019) showed that when the total solid-to-gas density ratio $\varepsilon \ll 1$ for a given dust-size distribution, the instability is as if being driven by the largest dust species alone. Therefore, as more and more discrete species N_{sp} are involved, the mass fraction of the leading species becomes smaller and smaller, resulting in increasingly small growth rate with increasing N_{sp} and hence its non-convergence. Counter-intuitively, as ε becomes significant, the growth of the instability with multiple species is even slower than the leading species in isolation would have driven. In this section, we use a different approach to explore this property in a different angle and attempt to gain some more insight into the role of the leading dust species and the interaction between the species.

Our experiment is designed as follows. As in Section 2.1, we divide a given dust-size distribution $T_s \in [10^{-4}, T_{s,\max}]$ with total solid-to-gas density ratio ε into N_{sp} regular logarithmic bins, with either $N_{\text{sp}} = 512$ or $N_{\text{sp}} = 1024$. Each bin then has a solid-to-gas density ratio ε_j (equation (1)) and is represented by identical dust particles with dimensionless stopping time $T_{s,j}$, where $T_{s,1} < T_{s,2} < \dots < T_{s,N_{\text{sp}}}$. We begin with the bin with the largest dust species $T_{s,N_{\text{sp}}}$ and find the fastest growing mode assuming that it is the only species present in the distribution. Then, we activate the bin with the second-largest dust species $T_{s,N_{\text{sp}}-1}$ in the distribution and find the fastest growing mode again for this case. In this manner, we systematically add more and more smaller dust species until we recover the full distribution.

The results for various $T_{s,\max}$, ε , and q are shown in Fig. 11. Comparing the black dots ($N_{\text{sp}} = 512$) with the red dots ($N_{\text{sp}} =$

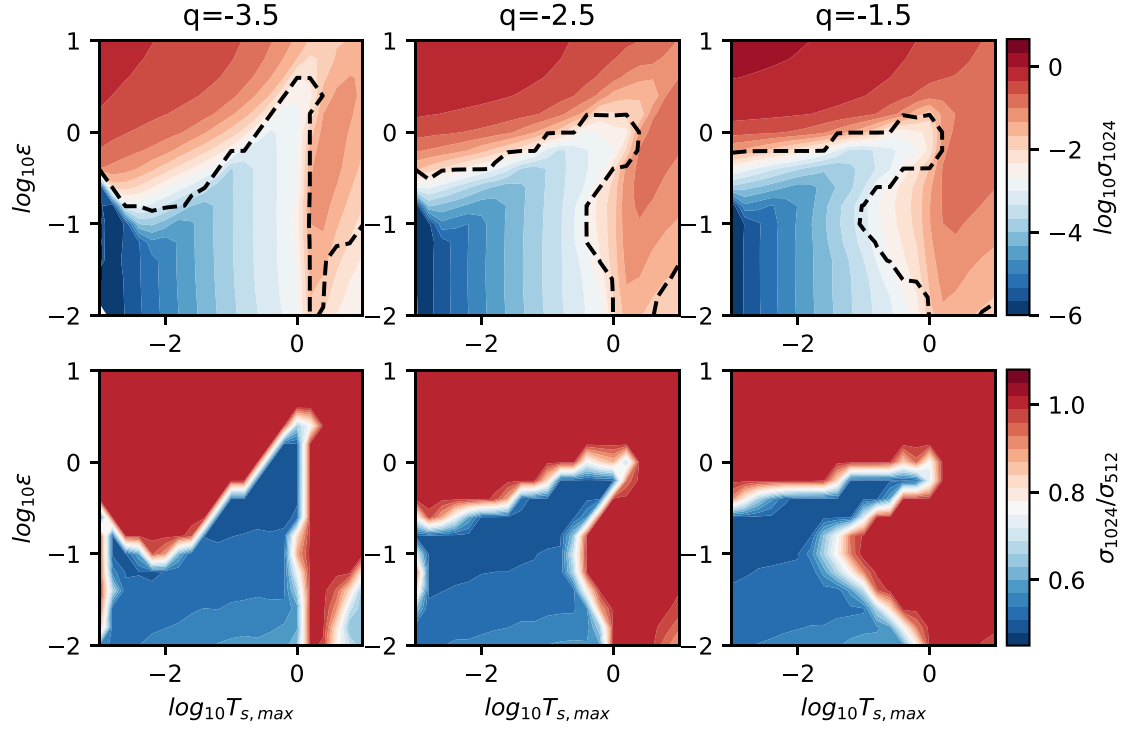


Figure 10. Similar to Fig. 1 but only the unstable modes with $k_z \geq 1/H_0$ are considered.

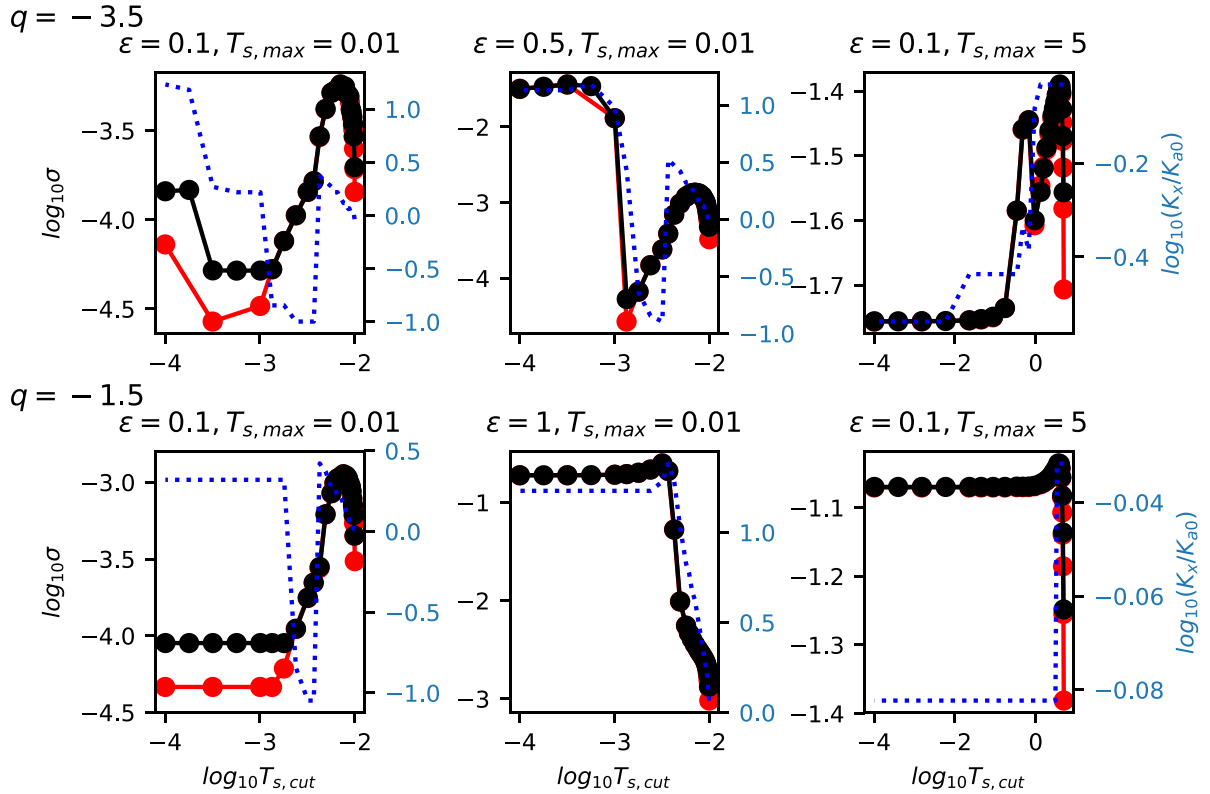


Figure 11. Maximum growth rate σ (dots; left-axis) and dimensionless radial wavenumber K_x (dotted lines; right-axis) as a function of the lower cutoff from a given dust-size distribution. Each panel represents a distribution with given dimensionless stopping time $T_s \in [10^{-4}, T_{s,\max}]$, power-law index q , and total solid-to-gas ratio ϵ , and the horizontal axis is the minimum stopping time $T_{s,\text{cut}}$ cut from such a distribution. The upper panels and the lower panels have $q = -3.5$ and -1.5 , respectively. The black dots mean the full distribution contains 512 dust species, while the red dots 1024 species. The blue curves are the K_x of the fastest mode with 512 dust species.

1024),⁴ it can be seen that the growth rate remains similar between the two cases when the lower cutoff of the distribution is high ($T_{s, \text{cut}} \gtrsim 10^{-3}$). When $T_{s, \text{cut}} \lesssim 10^{-3}$, the left-hand panels show smaller growth rates with $N_{\text{sp}} = 1024$ than with $N_{\text{sp}} = 512$, indicating non-convergence, while the middle and the right-hand panels continue to show consistent growth rates between $N_{\text{sp}} = 512$ and 1024, indicating convergence. Therefore, the two distinct regimes of convergence and non-convergence shown in Fig. 1 are only manifested when sufficiently small dust species are included.

Moreover, it is not apparent that the largest particles alone can determine the maximum growth rate of multiple dust species in a distribution. The smaller particles contribute to the instability in a sophisticated way. As shown in Fig. 11, the growth rate first increases when the next largest particles are activated in the distribution in both convergent and non-convergent cases. This can be understood as particles near $\sim T_{s, \text{max}}$ contribute constructively to the instability. This trend continues until $T_{s, \text{cut}} \simeq 0.7T_{s, \text{max}}$ at which the growth rate reaches maximum except the case of $\varepsilon = 1$, $T_{s, \text{max}} = 0.01$, and $q = -1.5$ whose rate reaches maximum at $T_{s, \text{cut}} \simeq 0.3T_{s, \text{max}}$. When even smaller particles are included, however, they can either constructively or destructively contribute to the instability. We note also that the radial wavenumber often begins near the resonant drag regime $K_x \sim K_{a0}$ and shifts to the region with larger K_x when sufficiently small dust particles are included (see Section 4.1).

Overall, it is apparent that the small dust particles (e.g. $T_s \lesssim 10^{-3}$) in a given distribution can have a strong effect on the instability, either positively or negatively. The combined mass for dust with stopping times between T_a and T_b is

$$\frac{m(T_a < T < T_b)}{m_{\text{total}}} = \frac{T_b^{4+q} - T_a^{4+q}}{T_{s, \text{max}}^{4+q} - 10^{-4(4+q)}}. \quad (4)$$

Therefore, dust with $T_s \leq 10^{-3}$ constitutes 24 per cent of the total dust mass for $T_{s, \text{max}} = 0.01$ and $q = -3.5$ (upper panels) or only 0.3 per cent of the total dust mass for $T_{s, \text{max}} = 0.01$ and $q = -1.5$ (lower panels). It can be seen that, in the top middle panel, the growth rate jumps significantly at $T_{s, \text{cut}} \simeq 10^{-3}$, which accompanies a sudden change of K_x . This indicates that the most unstable mode suddenly jumps from one K_x - K_z region to another region, and the contributions from the smaller particles may not simply be proportional. In this regard, it is not necessary that the instability can be considered as if being driven by the largest dust particles, or that the smaller dust particles can only contribute to the instability negatively, as suggested by Krapp et al. (2019).

To further demonstrate the differences between the streaming instability of multiple dust species and of one dust species representing the largest particle bin in a distribution alone, we consider the same $T_{s, \text{max}}-\varepsilon$ space for our dust distributions as in Section 3 but find the fastest growing mode for the latter scenario. These two scenarios are compared in Fig. 12. We have adopted $N_{\text{sp}} = 1024$ in the left-hand panels. Although the growth rates are both low at the small T_s and ε corner and both high at the large T_s and ε corner, they differ at low T_s and high ε . More importantly, the fastest growing mode with single species is located at $K_x = K_{a,0}$ as expected (lower right-hand panel), but is significantly different from the one with multiple species (lower left-hand panel). Therefore, the leading dust species does not appear to be acting independently in most of the parameter space we have considered.

⁴Due to the high computational cost with more dust species, we have picked a smaller $T_{s, \text{cut}}$ sample with $N_{\text{sp}} = 1024$ and hence fewer red points.

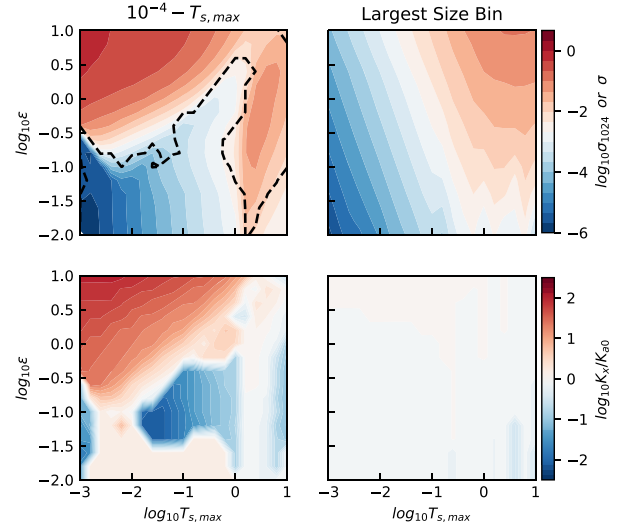


Figure 12. Left-hand panels: similar to the $q = -3.5$ case in Fig. 1 but derived by searching a wider K_x - K_z domain (Section 4.3). Right-hand panels: The maximum growth rate σ and the dimensionless radial wavenumber K_x of the most unstable mode for the single species whose ε and T_s are from the largest size bin in the dust distribution used in the left-hand panels.

4.3 Long-wavelength modes with $T_{s, \text{max}} \lesssim 1$ and $\varepsilon \lesssim 1$

We note that for some cases, the K_x - K_z domain, we use to search for the fastest growing modes may be too restrictive. This occurs near $T_{s, \text{max}} \lesssim 1$ and $\varepsilon \lesssim 1$, i.e. around the blue region in the bottom panels of Fig. 1. Fig. 8 suggests that the fastest growing modes are potentially located at even smaller K_x and K_z than we have considered. Therefore, we repeat some of the previous calculations in this section with a larger search domain that extends into two orders of magnitude smaller wavenumbers (see Section 2.1).

The results for dust distributions with $T_{s, \text{min}} = 10^{-4}$ but with different $q = -3.5$ and -1.5 are shown in the left-most panels of Figs 13 and 14, respectively. By comparing with the top left- and the top right-hand panels in Fig. 1, it can be seen that the fast-growth and the slow-growth regimes remain similar. However, comparing the middle panels indicates that the region with convergent maximum growth rate is enlarged near $T_{s, \text{max}} \lesssim 1$ and $\varepsilon \lesssim 1$. This difference is due to the capture of the much smaller wavenumbers, as shown by comparing the bottom panels. Nevertheless, these long-wavelength modes remain slowly growing, may not fit into the thickness of a vertically stratified disc, and hence are not quite relevant in the context of protoplanetary discs (cf. Fig. 10).

4.4 Narrow dust-size distributions

All our previous calculations assume that $T_{s, \text{max}}$ and $T_{s, \text{min}}$ ($T_{s, \text{min}} = 10^{-3}$ or 10^{-4}) are well separated. However, one could argue that dust grows preferentially to some characteristic sizes that are limited by growth barriers, so that $T_{s, \text{max}}$ and $T_{s, \text{min}}$ may be close to each other (e.g. Brauer, Dullemond & Henning 2008; Rozner, Grishin & Perets 2020). Furthermore, bringing $T_{s, \text{min}}$ closer to $T_{s, \text{max}}$ helps to shed some light on how the streaming instability with multiple species may make the transition into being considered as one with single species. In this section, therefore, we vary $T_{s, \text{min}}$ as a fraction of $T_{s, \text{max}}$ and the results are shown in Figs 13 and 14 for two different power-law index q .

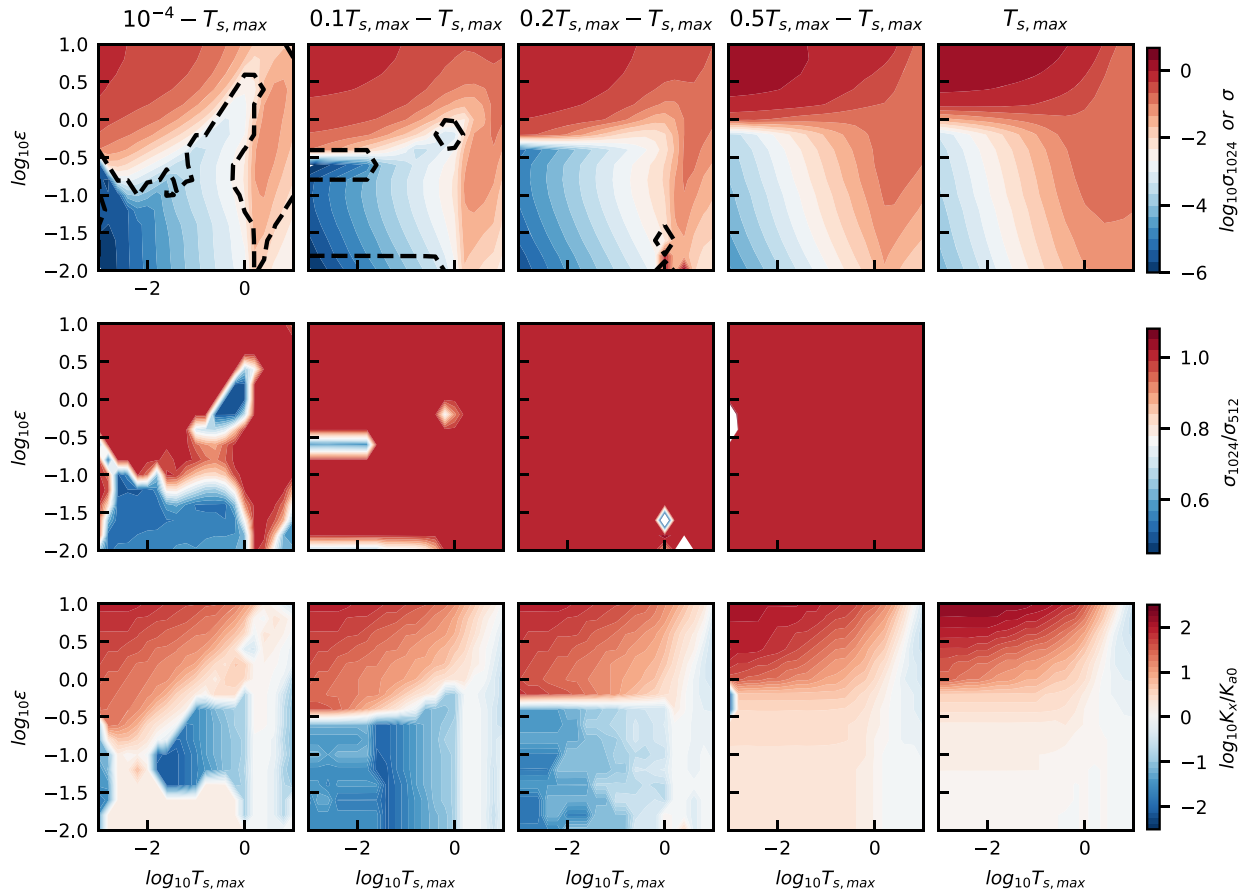


Figure 13. Similar to Fig. 1 but with different $T_{s, \min}$. All dust distributions have $q = -3.5$. The rightmost panels show the most unstable modes with the single dust species at $T_s = T_{s, \max}$. All the calculations use an extended K_x - K_z search space for the fastest growing mode (Section 4.3).

We find that a dust-size distribution need to be particularly narrow before it can be considered similar to a system with single species. As shown by the top panels in Figs 13 and 14, the sharp boundary between the fast and the slow growth regimes ($T_{s, \max} \sim 1$ and $\epsilon \sim 1$) remains apparent with $T_{s, \min}$ up to about $0.2T_{s, \max}$. This implies that, even with a dust-size distribution as narrow as ~ 0.7 dex, the dust particles do not interact coherently for the instability, and the unstable modes remain significantly different from those driven by single species. Only when $T_{s, \min} \gtrsim 0.5T_{s, \max}$, it can be seen that all the dust act coherently and the growth rate becomes similar to that from single species. Note that all these calculates have adopted 512 and 1024 dust species except the rightmost panels.

Another interesting trend is that the growth rate converges with the number of dust species N_{sp} in almost the entire $T_{s, \max}$ - ϵ domain when $T_{s, \min} \gtrsim 0.1T_{s, \max}$ (see the middle panels of Figs 13 and 14). Thus, unlike previous cases of wide dust-size range where the fast and slow growth rates are in the converged and non-converged regimes separately, both fast and slow growth rates are converged with the number of dust species when $T_{s, \min}$ is close to $T_{s, \max}$.

These results are consistent with Fig. 11 (discussed in Section 4.2) where adding particles with $T_s \gtrsim 0.5T_{s, \max}$ act coherently to increase the growth rate of the instability while adding even smaller particles starts to show deviation from the coherence. Eventually, adding particles with $T_s \lesssim 0.2T_{s, \max}$ can result in non-converged growth rates with number of dust species (the left-hand panels in Fig. 11).

5 SUMMARY

We have conducted analytical calculations and direct numerical simulations to study the linear phase of the streaming instability with multiple dust species. We have explored various dust distributions with different maximum dust sizes $T_{s, \max}$, total solid-to-gas mass ratios ϵ , and power-law indices q . In general, the instability has a high growth rate when *either* the maximum size $T_{s, \max}$ *or* the total solid-to-gas mass ratio ϵ is high ($T_{s, \max} \gtrsim 1$ or $\epsilon \gtrsim 1$). Under these conditions, the growth rate is converged with an increasing number of dust species N_{sp} representing the distribution. By contrast, the growth rate in the complimentary region of the parameter space, i.e. $T_{s, \max} \lesssim 1$ and $\epsilon \lesssim 1$, is quite low as long as $T_{s, \min} \lesssim 0.2T_{s, \max}$. When $T_{s, \min}$ is 10^{-3} or 10^{-4} , the growth rate continues to decrease significantly in this ϵ - $T_{s, \max}$ space with successively larger N_{sp} , implying that the growth rate with the limit of a continuous dust size distribution can be even lower than our calculated rates. When the size distribution is as narrow as $T_{s, \min} \gtrsim 0.1T_{s, \max}$, the growth rate seems to converge, albeit low. For more top-heavy dust distributions (e.g. $q = -1.5$), there is a larger parameter space for high growth rates extending down to $T_{s, \max} \sim 0.1$ (but the fastest growing modes for $0.1 \lesssim T_{s, \max} \lesssim 1$ cases may not fit in the thickness of a protoplanetary disc). Overall, the growth rate is clearly separated into the fast and the slow regimes when multiple dust species have been considered as long as $T_{s, \min} \lesssim 0.2T_{s, \max}$.

We find that the transition between the converged (fast growth) and the non-converged (slow growth) regimes is excessively sharp when

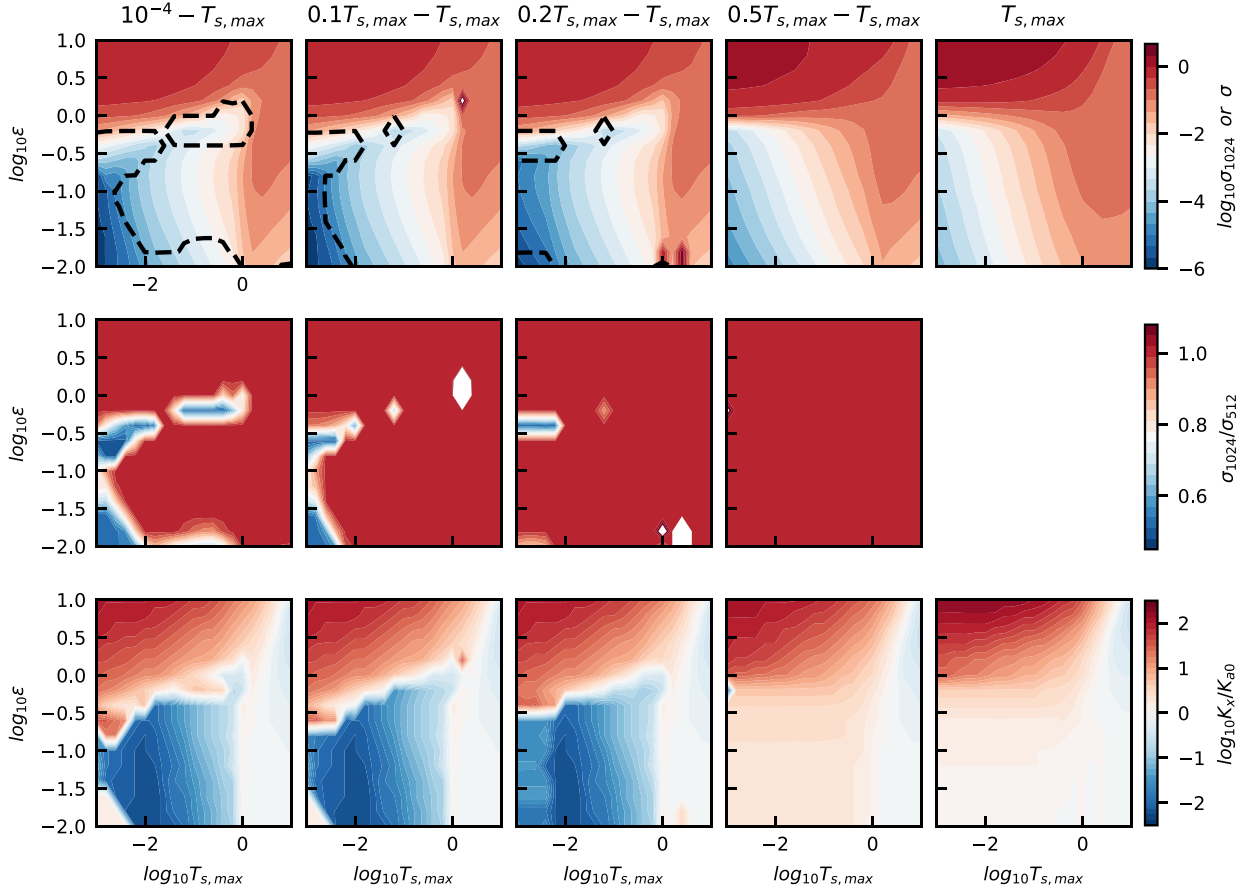


Figure 14. Similar to Fig. 13 but for dust distributions with $q = -1.5$.

$T_{s, \min} = 10^{-4}$. The more dust species N_{sp} , the sharper the transition becomes. Therefore, the growth rate map with respect to $T_{s, \max}$ and ϵ is clearly separated into converged and non-converged regions by a discontinuity-like boundary (Figs 1 and 2). Interestingly, for $\epsilon \gtrsim 1$, the most unstable mode in the converged region has a dimensionless radial wavenumber $K_x \gtrsim 10K_{a0}$, which is in a different branch from $K_x \sim K_{a0}$ identified as the resonant drag instability driven by the largest species (Squire & Hopkins 2018). For $\epsilon \lesssim 1$ and $T_{s, \max} \gtrsim 0.1$, on the other hand, the most unstable mode in the converged region has a variety of K_x depending on $T_{s, \max}$. When $T_{s, \max} \gtrsim 1$, K_x is close to K_{a0} . When $T_{s, \max}$ is small ($0.1 \lesssim T_{s, \max} \lesssim 1$), the fastest growing mode has $K_x \ll K_{a0}$, but these modes also have small K_z such that they cannot fit into typical disc thickness and should not operate in protoplanetary discs.

We also notice that, for a disc with a given ϵ and $T_{s, \max}$, only unstable modes in a limited range of wavenumbers have converged non-zero growth rates with an increasing number of dust species N_{sp} . Thus, when the disc condition changes (either ϵ or $T_{s, \max}$), the most unstable mode can move from outside the converged K_x – K_z region into the converged region. In this case, the growth rate of the instability changes from being non-convergent to convergent. This may help explain the sharp transition between the converged and the non-converged regions in the ϵ – $T_{s, \max}$ growth rate maps.

Different dust species in a distribution appear to interact and contribute to the instability in non-trivial ways. We find that for a wide range of conditions, the dynamics may not be simplified to the one

driven by the largest species in isolation, as may have been suggested by Bai & Stone (2010), Schaffer, Yang & Johansen (2018), and Krapp et al. (2019). Smaller dust species can either contribute positively or negatively to the instability. Moreover, they can change the relative importance of the unstable modes between different branches in the Fourier space to which the growth rate depends on sensitively (Figs 8 and 9).

Finally, we have used hybrid numerical simulations to reproduce the unstable modes for several representative cases. Numerical convergence has been achieved in all cases, and the corresponding analytical growth rates down to unprecedentedly low $\sigma \simeq 10^{-3}\Omega_K$ as well as for large leading species ($T_{s, \max} \sim 2$) are recovered. In the process, we have demonstrated the resolution requirement for simulating the instability with the code, which generally lies within 16–64 grid points per wavelength of the unstable modes. This experiment will serve us for future investigations of the streaming instability with multiple dust species using direct numerical simulations.

ACKNOWLEDGEMENTS

All simulations are carried out using computer supported by the Texas Advanced Computing Center (TACC) at The University of Texas at Austin through XSEDE grant TG-AST130002 and from the NASA High-End Computing (HEC) Program through the NASA Advanced Supercomputing (NAS) Division at Ames Research Center. ZZ acknowledges support from the National Science Foundation under

CAREER Grant Number AST-1753168 and NASA TCAN award 80NSSC19K0639. C-CY is grateful for the support from NASA via the Emerging Worlds program (Grant #80NSSC20K0347). We thank Leonardo Krapp, Andrew Youdin, and other TCAN members for constructive comments during the 2019 Tucson TCAN meeting and subsequent discussions/comments.

DATA AVAILABILITY

The data underlying this paper are available in the paper and in its online supplementary material.

REFERENCES

- Adachi I., Hayashi C., Nakazawa K., 1976, *Prog. Theor. Phys.*, 56, 1756
- Ansdell M. et al., 2016, *ApJ*, 828, 46
- Bai X.-N., Stone J. M., 2010, *ApJS*, 190, 297
- Bai X.-N., Stone J. M., 2014, *ApJ*, 796, 31
- Balsara D. S., Tilley D. A., Rettig T., Brittain S. D., 2009, *MNRAS*, 397, 24
- Barge P., Sommeria J., 1995, *A&A*, 295, L1
- Benítez-Llambay P., Krapp L., Pessah M. E., 2019, *ApJS*, 241, 25
- Benz W., Asphaug E., 1999, *Icarus*, 142, 5
- Birnstiel T., Klahr H., Ercolano B., 2012, *A&A*, 539, A148
- Birnstiel T., Fang M., Johansen A., 2016, *Space Sci. Rev.*, 205, 41
- Blum J., Wurm G., 2008, *ARA&A*, 46, 21
- Brandenburg A., Dobler W., 2002, *Comput. Phys. Commun.*, 147, 471
- Brauer F., Dullemond C. P., Henning T., 2008, *A&A*, 480, 859
- Bukhari Syed M., Blum J., Wahlberg Jansson K., Johansen A., 2017, *ApJ*, 834, 145
- Carrera D., Johansen A., Davies M. B., 2015, *A&A*, 579, A43
- Chen K., Lin M.-K., 2020, *ApJ*, 891, 132
- Garaud P., Barrière-Fouchet L., Lin D. N. C., 2004, *ApJ*, 603, 292
- Gerbig K., Murray-Clay R. A., Klahr H., Baehr H., 2020, *ApJ*, 895, 91
- Gole D. A., Simon J. B., Li R., Youdin A. N., Armitage P. J., 2020, *ApJ*, 904, 132
- Johansen A., Youdin A., 2007, *ApJ*, 662, 627
- Johansen A., Youdin A., Klahr H., 2009, *ApJ*, 697, 1269
- Johansen A., Blum J., Tanaka H., Ormel C., Bizzarro M., Rickman H., 2014, in Beuther H., Klessen R. S., Dullemond C. P., Henning T., eds, *Protostars and Planets VI*. University of Arizona Press, Tucson, AZ, p. 547
- Kataoka A., Tanaka H., Okuzumi S., Wada K., 2013, *A&A*, 557, L4
- Klahr H., Schreiber A., 2020, *ApJ*, 901, 54
- Krapp L., Benítez-Llambay P., Gressel O., Pessah M. E., 2019, *ApJ*, 878, L30
- Leinhardt Z. M., Stewart S. T., 2009, *Icarus*, 199, 542
- Li R., Youdin A. N., Simon J. B., 2018, *ApJ*, 862, 14
- Lin M.-K., Youdin A. N., 2017, *ApJ*, 849, 129
- Lyra W., Johansen A., Klahr H., Piskunov N., 2009, *A&A*, 493, 1125
- Mathis J. S., Rumpl W., Nordsieck K. H., 1977, *ApJ*, 217, 425
- Michikoshi S., Kokubo E., Inutsuka S.-i., 2012, *ApJ*, 746, 35
- Mignone A., Flock M., Vaidya B., 2019, *ApJS*, 244, 38
- Miniati F., 2010, *J. Comput. Phys.*, 229, 3916
- Nakagawa Y., Sekiya M., Hayashi C., 1986, *Icarus*, 67, 375
- Pérez L. M. et al., 2015, *ApJ*, 813, 41
- Rozner M., Grishin E., Perets H. B., 2020, *MNRAS*, 496, 4827
- San Sebastián I. L., Dolff A., Blum J., Parisi M. G., Kothe S., 2020, *MNRAS*, 497, 2418
- Schaffer N., Yang C.-C., Johansen A., 2018, *A&A*, 618, A75
- Squire J., Hopkins P. F., 2018, *MNRAS*, 477, 5011
- Takahashi S. Z., Inutsuka S.-i., 2014, *ApJ*, 794, 55
- Umurhan O. M., Estrada P. R., Cuzzi J. N., 2020, *ApJ*, 895, 4
- Weidenschilling S. J., 1977, *MNRAS*, 180, 57
- Whipple F. L., 1972, in Elvius A., ed., *From Plasma to Planet*, Wiley, New York, NY, p. 211
- Williams J. P., Cieza L. A., 2011, *ARA&A*, 49, 67
- Yang C. C., Johansen A., Carrera D., 2017, *A&A*, 606, A80
- Yang C.-C., Johansen A., 2014, *ApJ*, 792, 86
- Yang C.-C., Johansen A., 2016, *ApJS*, 224, 39
- Yang C.-C., Krumholz M., 2012, *ApJ*, 758, 48
- Yang C.-C., Mac Low M.-M., Johansen A., 2018, *ApJ*, 868, 27
- Youdin A. N., 2011, *ApJ*, 731, 99
- Youdin A. N., Goodman J., 2005, *ApJ*, 620, 459
- Youdin A., Johansen A., 2007, *ApJ*, 662, 613
- Zsom A., Ormel C. W., Güttler C., Blum J., Dullemond C. P., 2010, *A&A*, 513, A57

APPENDIX A: SEEDING DENSITY PERTURBATIONS BY LAGRANGIAN PARTICLES

Youdin & Johansen (2007) in their Appendix C described how to seed a sinusoidal perturbation in density with Lagrangian particles. When there exist multiple perturbations with an arbitrary phase, cross correction terms are needed to maintain high order of accuracy. In this appendix, we illustrate how this can be achieved.

Following Youdin & Johansen (2007), we consider the superposition of two waves with wavenumbers $\mathbf{k}_{\pm} \equiv k_{x,0}\hat{\mathbf{e}}_x \pm k_{z,0}\hat{\mathbf{e}}_z$, resulting in one horizontally propagating but vertically standing wave. In this case, the initial density field of the particles in the xz -plane reads (see their equation 10a)

$$\rho_p(\mathbf{r}) = \rho_0 [1 + (A_R \cos k_{x,0}x - A_I \sin k_{x,0}x) \cos k_{z,0}z] \quad (\text{A1})$$

$$= \rho_0 \left[1 + \frac{1}{2} A_R (\cos \mathbf{k}_+ \cdot \mathbf{r} + \cos \mathbf{k}_- \cdot \mathbf{r}) - \frac{1}{2} A_I (\sin \mathbf{k}_+ \cdot \mathbf{r} + \sin \mathbf{k}_- \cdot \mathbf{r}) \right], \quad (\text{A2})$$

where $\mathbf{r} \equiv x\hat{\mathbf{e}}_x + z\hat{\mathbf{e}}_z$ is the position, ρ_0 is the mean density, $A \equiv A_R + iA_I$ is the complex amplitude of the waves relative to ρ_0 .

To approximate the continuous density field (equation A1) using discrete particles, we begin with a periodic domain accommodating integral numbers of wavelengths $\lambda_{x,0} \equiv 2\pi/k_{x,0}$ and $\lambda_{z,0} \equiv 2\pi/k_{z,0}$ in both directions. We uniformly distribute N_p identical particles with positions \mathbf{r}_j and shift the position of each particle by ξ_j . The density field of the particles is then

$$\rho_p(\mathbf{r}) = m_p \sum_j \delta(\mathbf{r} - \mathbf{r}_j - \xi_j), \quad (\text{A3})$$

where m_p is the mass of each particle and $\delta(\mathbf{r})$ is the Dirac δ function.⁵ Fourier transforming equation (A3) over the domain gives

$$\tilde{\rho}_p(\mathbf{k}) = m_p \sum_j \exp(i\mathbf{k} \cdot \mathbf{r}_j) \left[1 + i\mathbf{k} \cdot \boldsymbol{\xi}_j - \frac{1}{2} (\mathbf{k} \cdot \boldsymbol{\xi}_j)^2 + O(|\mathbf{k} \cdot \boldsymbol{\xi}_j|^3) \right]. \quad (\text{A4})$$

Equation (A2) suggests that to first order in $|A|$, the position shifts should be

$$\boldsymbol{\xi}_j^{(1)} = -\frac{A_R}{2k_0^2} (\mathbf{k}_+ \sin \mathbf{k}_+ \cdot \mathbf{r}_j + \mathbf{k}_- \sin \mathbf{k}_- \cdot \mathbf{r}_j) - \frac{A_I}{2k_0^2} (\mathbf{k}_+ \cos \mathbf{k}_+ \cdot \mathbf{r}_j + \mathbf{k}_- \cos \mathbf{k}_- \cdot \mathbf{r}_j), \quad (\text{A5})$$

where $k_0 \equiv \sqrt{k_{x,0}^2 + k_{y,0}^2}$. Substituting $\boldsymbol{\xi}_j = \boldsymbol{\xi}_j^{(1)}$ into equation (A4) results in

$$\begin{aligned} \tilde{\rho}_p(\mathbf{k}) = N_p m_p & \left[1 + \frac{1}{4} A_R (\delta_{\mathbf{k},+\mathbf{k}_+} + \delta_{\mathbf{k},-\mathbf{k}_+} + \delta_{\mathbf{k},+\mathbf{k}_-} + \delta_{\mathbf{k},-\mathbf{k}_-}) - \frac{i}{4} A_I (\delta_{\mathbf{k},+\mathbf{k}_+} - \delta_{\mathbf{k},-\mathbf{k}_+} + \delta_{\mathbf{k},+\mathbf{k}_-} - \delta_{\mathbf{k},-\mathbf{k}_-}) \right. \\ & + \frac{1}{8} (A_R^2 - A_I^2) (\delta_{\mathbf{k},+2\mathbf{k}_+} + \delta_{\mathbf{k},-2\mathbf{k}_+} + \delta_{\mathbf{k},+2\mathbf{k}_-} + \delta_{\mathbf{k},-2\mathbf{k}_-}) - \frac{i}{4} A_R A_I (\delta_{\mathbf{k},+2\mathbf{k}_+} - \delta_{\mathbf{k},-2\mathbf{k}_+} + \delta_{\mathbf{k},+2\mathbf{k}_-} - \delta_{\mathbf{k},-2\mathbf{k}_-}) \\ & + \frac{1}{4} (A_R^2 + A_I^2) \left(\frac{k_{z,0}}{k_0} \right)^4 (\delta_{\mathbf{k},+2k_{z,0}\hat{e}_z} + \delta_{\mathbf{k},-2k_{z,0}\hat{e}_z}) + \frac{1}{4} (A_R^2 - A_I^2) \left(\frac{k_{x,0}}{k_0} \right)^4 (\delta_{\mathbf{k},+2k_{x,0}\hat{e}_x} + \delta_{\mathbf{k},-2k_{x,0}\hat{e}_x}) \\ & \left. - \frac{i}{2} A_R A_I \left(\frac{k_{x,0}}{k_0} \right)^4 (\delta_{\mathbf{k},+2k_{x,0}\hat{e}_x} - \delta_{\mathbf{k},-2k_{x,0}\hat{e}_x}) + O(|A|^3) \right], \quad (\text{A6}) \end{aligned}$$

where $\delta_{\mathbf{u},\mathbf{v}} \equiv \delta(\mathbf{u} - \mathbf{v})$ for any \mathbf{u} and \mathbf{v} . In other words, perturbations of amplitude on the order of $|A|^2$ appear in the second harmonics. These overtones can be cancelled by introducing the second-order correction shifts

$$\begin{aligned} \boldsymbol{\xi}_j^{(2)} = & \frac{A_R^2 - A_I^2}{8k_0^2} (\mathbf{k}_+ \sin 2\mathbf{k}_+ \cdot \mathbf{r}_j + \mathbf{k}_- \sin 2\mathbf{k}_- \cdot \mathbf{r}_j) + \frac{A_R A_I}{4k_0^2} (\mathbf{k}_+ \cos 2\mathbf{k}_+ \cdot \mathbf{r}_j + \mathbf{k}_- \cos 2\mathbf{k}_- \cdot \mathbf{r}_j) \\ & + \frac{(A_R^2 + A_I^2) k_{z,0}^3}{4k_0^4} \hat{e}_z \sin 2k_{z,0} z_j + \frac{(A_R^2 - A_I^2) k_{x,0}^3}{4k_0^4} \hat{e}_x \sin 2k_{x,0} x_j + \frac{A_R A_I k_{x,0}^3}{2k_0^4} \hat{e}_x \cos 2k_{x,0} x_j. \quad (\text{A7}) \end{aligned}$$

⁵We note that any of the weighting schemes of the particle-mesh method has the properties of a δ function.